ALIEN EARTHS

Which Nearby Planetary Systems Are Likely to
Host Habitable Planets and Life?

MONTHLY NEWSLETTER

September 2025

ALIEN EARTHS

Alien Earths is part of NASA's Nexus for Exoplanetary System Science program, which carries out coordinated research toward the goal of searching for and determining the frequency of habitable extrasolar planets with atmospheric biosignatures in the Solar neighborhood.

Our interdisciplinary teams includes astrophysicists, planetary scientists, cosmochemists, material scientists, chemists, biologists, and physicists.

The Principal Investigator of Alien Earths is Daniel Apai (University of Arizona). The projects' lead institutions are The University of Arizona's Steward Observatory and Lunar and Planetary Laboratory.

For a complete list of publications, please visit the AE Library on the SAO/NASA Astrophysics Data System.

Alien Earths is on social media!

facebook.com/alienearths.space

instagram.com/alienearths

linkedin.com/company/alienearths

x.com/alien_earths

Find us, follow us and share with your friends and colleagues. Send news and events to rstratton@arizona.edu to be shared across platforms.

Astronomers have long sought after views of forming planets. While forming planetary systems (i.e., the disks of gas and dust from which planets form) are frequently observed, the planets themselves largely remain elusive. Recently, astronomers on the Alien Earths team have caught a rare glimpse of forming planets in concert with the disk from which they formed. Professors Jared Males and Laird Close from the University of Arizona's Steward Observatory built the MagAO-X adaptive optics system (located in Chile) and used it to discover an accreting protoplanet, WISPIT-2b.
Afterward, Steward Observatory PhD student Gabriel Weible and Professor Kevin Wagner followed up the discovery with the LBTI instrument (located in Arizona) to observe thermal emission from the planet, pictured here. The two observations of the planet at different wavelengths enable measurements of both its temperature and the amount of gas being accreted by the planet as it undergoes its final stages of formation. The discovery of of WISPIT-2b adds to the handful of known protoplanets, and provides constraints for theoretical models of giant planet formation that can be used to understand both our own solar system and those around others stars.

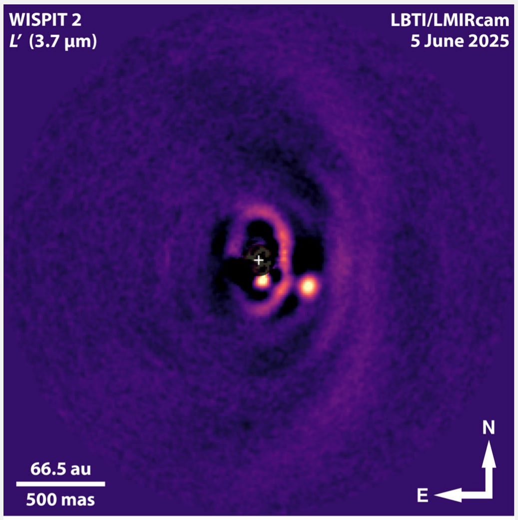

Welcome to the Group!

NOAH TUCHOW, Post Doctoral Research Associate
Noah'S research focuses on preparing for the next generation of space telescope missions to discover planets around other stars. Noah received his PhD in 2022 from Pennsylvania State University, where he focused on the effects of stellar evolution on the long-term habitability of exoplanets.

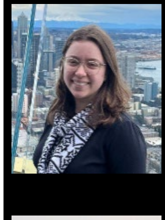

KYLIE HALL, Graduate Student
Kylie is a graduate student at the Lunar and Planetary Laboratory working with Dr. Daniel Apai on exoplanet habitability. She is currently focused on assessing how varying planetary characteristics impact an exoplanet's likelihood to be able to support different kinds of metabolisms.

Vivian Welch, Undergraduate Research Assistant
Vivian is an Undergraduate Software Developer for Bioverse. She manages the GitHub, ReadTheDocs, PyPi, testing and debugging of advancements, and drafting of new releases. Her research interests lie in the world of scientific computing, specifically quantum information science.

Rahul Rathore, Undergraduate Research Assistant
Rahul Rathore works on the Quantitative Habitability Framework (QHF), where he has focused on improving both functionality and usability for researchers. Rahul is a senior undergraduate student at the University of Arizona .

Recent Publications

A Multispecies Atmospheric Escape Model with Excited Hydrogen and Helium: Application to HD209458b

……………………………

The observable impact of runaway OB stars on protoplanetary discs

……………………………

The past, present and future of observations of externally irradiated disks

……………………………

Long-term X-Ray Variability on the Benchmark YSO HL Tau

……………………………

Smuggling unnoticed: towards a 2D view of water and dust delivery to the inner regions of protoplanetary discs

……………………………

Evidence for Variable Accretion onto PDS 70 c and Implications for Protoplanet Detections

……………………………

Three-dimensional Transport of Solids in a Protoplanetary Disk Containing a Growing Giant Planet

……………………………

The Doubly Librating Plutinos

……………………………

Tides on Lava Worlds: Application to Close-in Exoplanets and the Early Earth–Moon System

……………………………

Discovery and Characterization of an Eccentric, Warm Saturn Transiting the Solar Analog TOI-4994

……………………………

Three warm Jupiters orbiting TOI-6628, TOI-3837, and TOI-5027 and one sub-Saturn orbiting TOI-2328

……………………………

Characterization of seven transiting systems, including four warm Jupiters from SOPHIE and TESS

……………………………

Super-Earths and Earth-like Exoplanets

……………………………

History and Habitability of the LP 890-9 Planetary System

A Multispecies Atmospheric Escape Model with Excited Hydrogen and Helium: Application to HD209458b

Taylor, Anna Ruth; Koskinen, Tommi T.; Argenti, Luca; Lewis, Nicholas; Huang, Chenliang; Arfaux, Anthony; Lavvas, Panayotis

The Astrophysical Journal, Volume 989, Issue 1, id.68, 24 pp.

Atmospheric escape shapes exoplanet evolution and star–planet interactions, with He I 10830 Å absorption serving as a key tracer of mass loss in hot gas giants. However, transit depths vary significantly across observed systems for reasons that remain poorly understood. HD209458b, the archetypal hot-Jupiter, exhibits relatively weak He I 10830 Å and Hα absorption, which has been interpreted as evidence for a high H/He ratio (98/2), possibly due to diffusive separation. To investigate this possibility and other processes that control these transit depths, we reassess excitation and de-excitation rates for metastable helium and explore the impact of diffusion processes, stellar activity, and tidal forces on the upper atmosphere and transit depths using a model framework spanning the whole atmosphere. Our model reproduces the observed He I transit depth and Hα upper limit, showing strong diffusive separation. We match the observations assuming a photoelectron efficiency of 20%–40%, depending on the composition of the atmosphere, corresponding to mass-loss rates of 1.9–3 × 10^{10} g s^{-1}. We find that the He I 10830 Å transit depth is sensitive to both stellar activity and diffusion processes, while Hα is largely unaffected due to its strong dependence on Lyα excitation. These differences may help explain the system-to-system scatter seen in population-level studies of the He I line. While He I data alone may not tightly constrain mass-loss rates or temperatures, they do confirm atmospheric escape and help narrow the viable parameter space when interpreted with physically motivated models. Simultaneous observations of He I, Hα, and stellar activity indicators provide powerful constraints on upper atmosphere dynamics and composition, even in the absence of full transmission spectra.

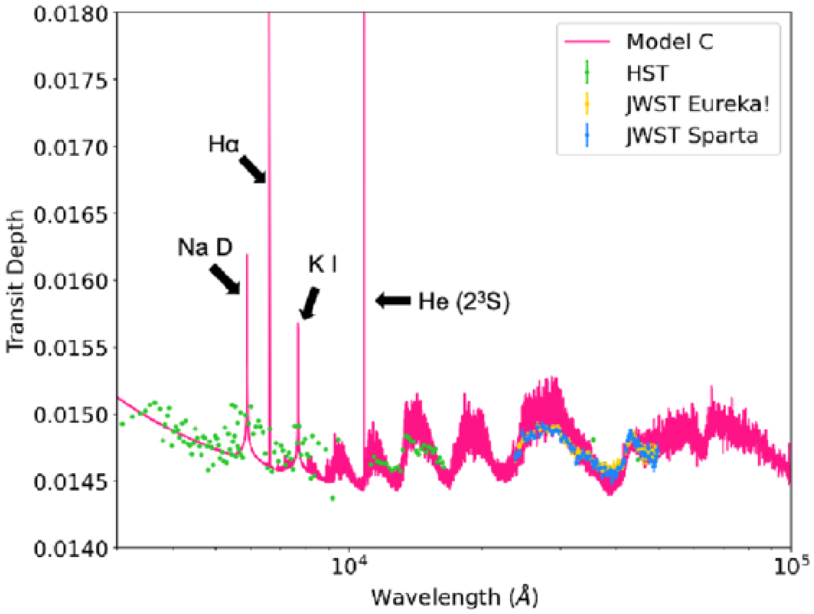

***Figure 9**. Transit depth vs. wavelength for our full atmosphere model of HD209458b (Model C). We zoom in past the extent of the Hα and He I 10830 Å line to show the comparison with HST observations (D. K. Sing et al. 2016) and JWST observations (with different data reduction pipelines in different colors; Q. Xue et al. 2024). The JWST observations analyzed can be accessed via DOI: 10.17909/h04g-kt93. Note that the Na D and K I lines are a result of only the lower/middle atmosphere model, and we do not calculate transit depths for these lines based on the upper atmosphere model.*

The observable impact of runaway OB stars on protoplanetary discs

Coleman, Gavin A. L; Kim, Jinyoung Serena; Haworth, Thomas J.; Hartman, Peter A.; Kalish, Taylor C.

➔ Monthly Notices of the Royal Astronomical Society, Volume 540, Issue 1, pp. 1202-1214, 13 pp.

Ultraviolet (UV) radiation from OB stars can drive 'external' photoevaporative winds from discs in clusters, that have been shown to be important for disc evolution and planet formation. However, cluster dynamics can complicate the interpretation of this process. A significant fraction of OB stars are runaways, propagating at high velocity which might dominate over the wider cluster dynamics in setting the time variation of the UV field in part of the cluster. We explore the impact of a runaway OB star on discs and the observational impact that may have. We find that discs exposed to even short periods of strong irradiation are significantly truncated, and only rebound slightly following the 'flyby' of the UV source. This is predicted to leave an observable imprint on a disc population, with those downstream of the OB star vector being more massive and extended than those upstream. Because external photoevaporation acts quickly, this imprint is less susceptible to being washed out by cluster dynamics for faster runaway OB stars. The Gaia proper motion vector of the B star 42 Ori in NGC 1977 is transverse to the low mass stellar population and so may make a good region to search for this signature in resolved disc observations.

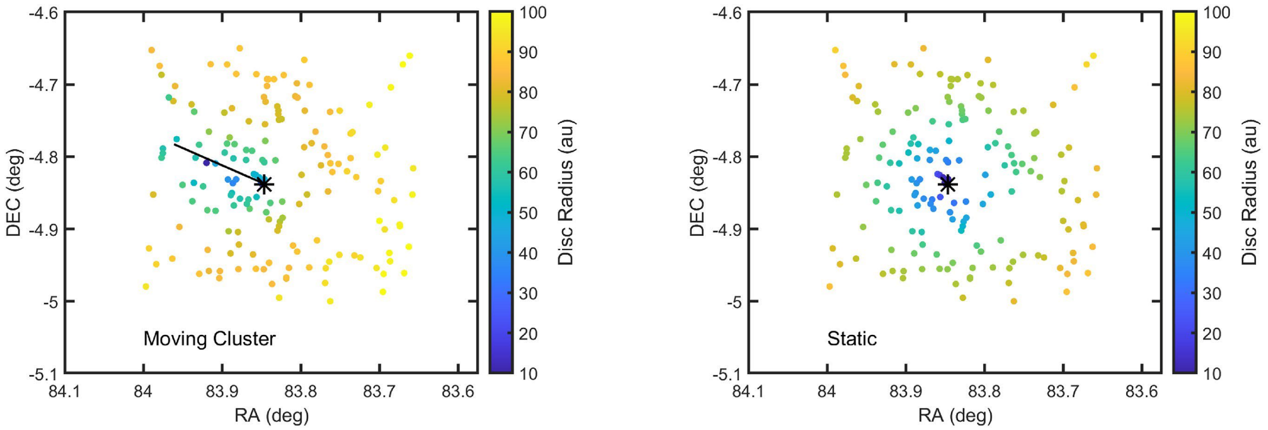

Figure 16. *Spatial coordinates of the stars in NGC 1977, with the colours showing the simulated disc radii after 2 Myr when all of the stars are moving in the cluster (left-hand panel), and when they are static (right-hand panel). The black star shows the current location of 42 Ori, with the solid black line in the left-hand panel showing its' trajectory over the last 100 Kyr. A movie of the left-hand panel showing the Moving Cluster can be found in the online supplementary material.*

The past, present and future of observations of externally irradiated disks

Allen, Megan; Anania, Rossella; Andersen, Morten; Aru, Mari-Liis; Ballabio, Giulia; Ballering, Nicholas P.; Beccari, Giacomo; Berné, Olivier; Bik, Arjan; Boyden, Ryan; Coleman, Gavin; Díaz-Berrios, Javiera; Eatson, Joseph W.; Frediani, Jenny; Forbrich, Jan; Gkimisi, Katia; Goicoechea, Javier R.; Gupta, Saumya; Guarcello, Mario G.; Haworth, Thomas J.; Henney, William J.; Isella, Andrea; Itrich, Dominika; Keyte, Luke; Kim, Jinyoung Serena; Kuhn, Michael; Le Petit, Frank; Luo, Lilian; Manara, Carlo; Mauco, Karina; Meshaka, Raphaël; Millstone, Samuel; Owen, James E.; Paine, Sébastien; Parker, Richard; Peake, Tyger; Peatt, Megan; Pinilla, Paola; Qiao, Lin; Ramírez-Tannus, María Claudia; Ramsay, Suzanne; Reiter, Megan; Rogers, Ciarán; Rosotti, Giovanni; Schroetter, Ilane; Sellek, Andrew; Testi, Leonardo; van Terwisga, Sierk; Vicente, Silvia; Walsh, Catherine; Winter, Andrew; Wright, Nicholas J.; Zeidler, Peter

➔ The Open Journal of Astrophysics, vol. 8, id. 54

Recent years have seen a surge of interest in the community studying the effect of ultraviolet radiation environment, predominantly set by OB stars, on protoplanetary disc evolution and planet formation. This is important because a significant fraction of planetary systems, potentially including our own, formed in close proximity to OB stars. This is a rapidly developing field, with a broad range of observations across many regions recently obtained or recently scheduled. In this paper, stimulated by a series of workshops on the topic, we take stock of the current and upcoming observations. We discuss how the community can build on this recent success with future observations to make progress in answering the big questions of the field, with the broad goal of disentangling how external photoevaporation contributes to shaping the observed (exo)planet population. Both existing and future instruments offer numerous opportunities to make progress towards this goal.

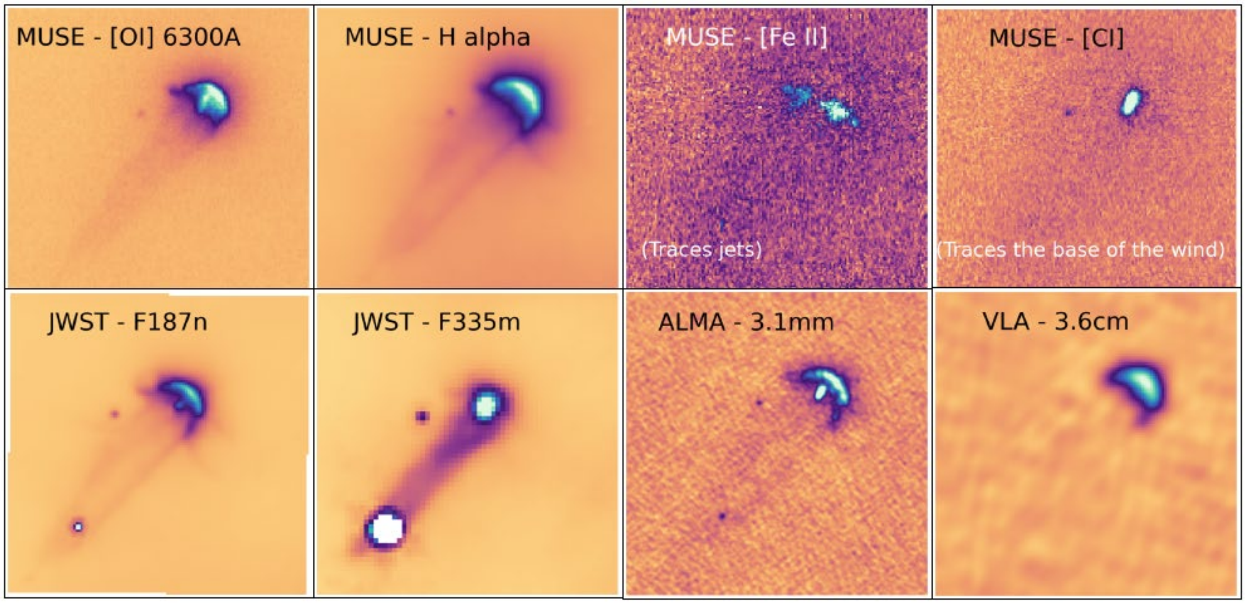

***Figure 1**. A gallery of images of the proplyd 177-341 in the ONC from different facilities…*

Long-term X-Ray Variability on the Benchmark YSO HL Tau

Silverberg, Steven M.; Wolk, Scott J.; Principe, David A.; Schneider, P. C.; Günther, Hans Moritz; Kim, Jinyoung Serena; Kastner, Joel H.

The Astronomical Journal, Volume 169, Issue 3, id.177, 12 pp.

HL Tau is one of the most well-studied Class I young stellar objects (YSOs), including frequent observations at near- and mid-infrared, (sub)millimeter, and X-ray wavelengths. We present the results of an X-ray variability monitoring campaign with XMM-Newton in 2020 and X-ray grating spectroscopy from Chandra/HETGS in 2018. We find that the X-ray spectrum of HL Tau is consistently hot (with characteristic plasma temperatures T $\gtrsim$ 30 MK) over 31 epochs spanning 20 yr, which is consistent in temperature with most Class I YSOs. The high-resolution HETG spectrum indicates the presence of some cooler plasma. We characterize the variability of the star across the 31 observations and find a subset of observations with significant variability on a ~21-day timescale in the observed count rate and flux. We discuss the possible origins of this variability and identify further observations that would better constrain the nature of the changes.

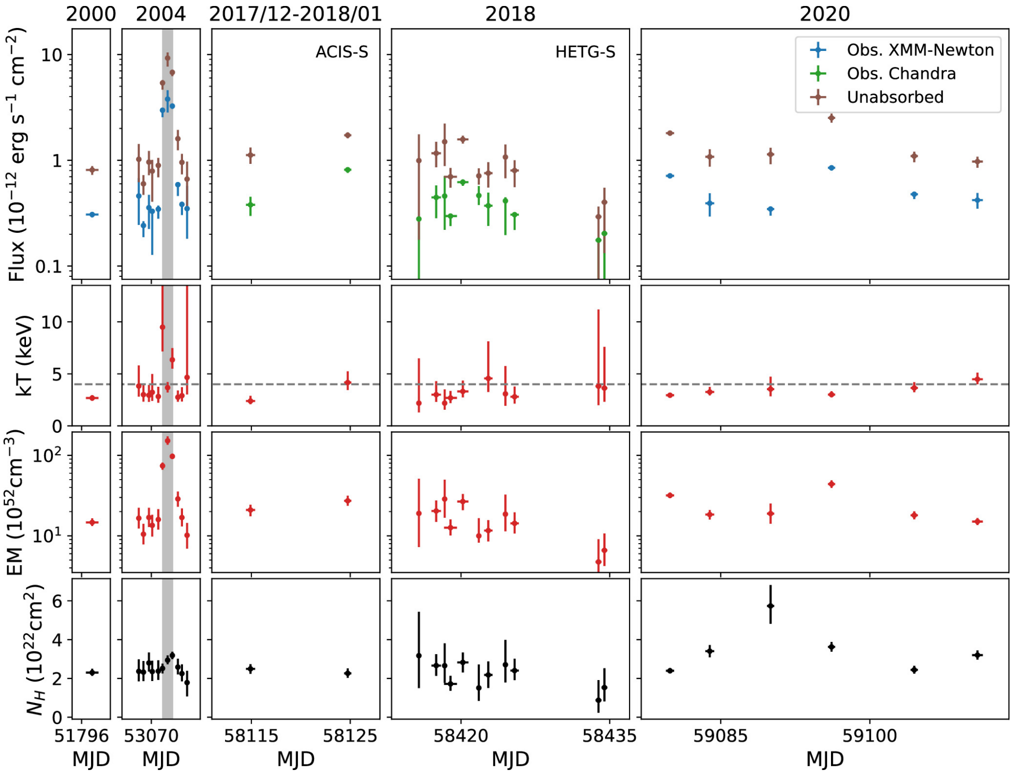

***Figure 9**. Comparison of model fits to HL Tau observations from 2000 to 2020. All models use one APEC plasma component with variable temperature and a fixed abundance for Fe (and elements with Fe-like FIP) set at the best-fit value from a joint fit to the faint XMM-Newton observations from 2020 and a variable absorption component. Top row: flux is shown both absorbed (as observed; blue for XMM-Newton, green for Chandra) and unabsorbed (corrected for N_H; brown). Second row: the plasma temperature for the single plasma component (red) in comparison to 4 keV. Third row: the emission measure for the single plasma component (red). Bottom row: the column density N_H of the absorbing material (black). Observing windows are labeled above each column. The observations during the flare identified by G. Giardino et al. (2006) in 2004 are highlighted in gray.*

Smuggling unnoticed: towards a 2D view of water and dust delivery to the inner regions of protoplanetary discs

Houge, Adrien; Krijt, Sebastiaan; Banzatti, Andrea; Blake, Geoffrey A; Pinilla, Paola; Pontoppidan, Klaus M; Trapman, Leon; Williams, Joe; Zhang, Ke

Monthly Notices of the Royal Astronomical Society, Volume 537, Issue 2, pp.691-704

Infrared spectroscopy, e.g. with JWST, provides a glimpse into the chemical inventory of the innermost region of protoplanetary discs, where terrestrial planets eventually form. The chemical make-up of regions inside snowlines is connected to the material drifting from the outer regions, which can be modelled with dust evolution models. However, infrared observations are limited by the high dust extinction in the inner disc, and only probes the abundances of gaseous species in the disc surface layers. As a result, the bulk mass of delivered volatiles is not directly relatable to what is measured through infrared spectra. In this paper, we investigate how the delivery of dust and ice after prolonged pebble drift affects the observable reservoir of water vapour in the inner disc. We develop a 1 + 1D approach based on dust evolution models to determine the delivery and distribution of vapour compared to the height of the τ=1 surface in the dust continuum. We find that the observable column density of water vapour at wavelengths probed by JWST spans many orders of magnitude over time, exhibiting different radial profiles depending on dust properties, drift rate, and local processing. In the presence of a traffic-jam effect inside the snowline, the observable vapour reservoir appears constant in time despite the ongoing delivery by pebble drift, such that water is effectively smuggled unnoticed. Differences in measured column densities then originate not only from variations in bulk vapour content, but also from differences in the properties and distribution of dust particles.

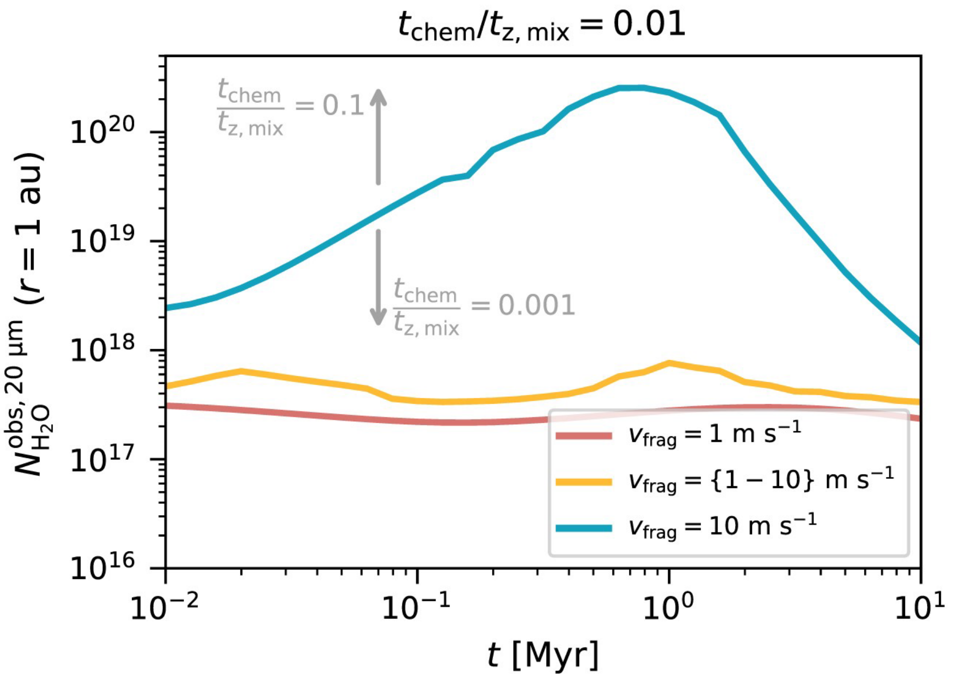

Figure 6. *Observable column density of water vapour abo v e the τ20 μm = 1 surface of the dust continuum at 1 au , as a function of time for three dust models, assuming t chem /t z , mix = 0 . 01 (efficient UV and chemical processing of vapour).*

Evidence for Variable Accretion onto PDS 70 c and Implications for Protoplanet Detections

Zhou, Yifan; Bowler, Brendan P.; Sanghi, Aniket; Marleau, Gabriel-Dominique; Takasao, Shinsuke; Aoyama, Yuhiko; Hasegawa, Yasuhiro; Thanathibodee, Thanawuth; Uyama, Taichi; Hashimoto, Jun; Wagner, Kevin; Calvet, Nuria; Demars, Dorian; Wu, Ya-Lin; Biddle, Lauren I.; Haffert, Sebastiaan Y.; Bryan, Marta L.

The Astrophysical Journal Letters, Volume 980, Issue 2, id.L39, 9 pp.

Understanding the processes of planet formation and accretion in young systems is essential to unraveling the initial conditions of planetary systems. The PDS 70 system, which hosts two directly imaged protoplanets, provides a unique laboratory for studying these phenomena, particularly through Hα emission, a commonly used accretion tracer. We present multiepoch observations and examine the variability in accretion signatures within this system, focusing on PDS 70 b and c. Using Hubble Space Telescope narrowband Hα imaging data taken in 2020 and 2024, we achieve high signal-to-noise ratio detections of these planets and reveal significant changes in Hα flux. For PDS 70 c, the Hα flux more than doubled between 2020 and 2024. The trend is consistent with the one identified in recently published MagAO-X data, further confirming that PDS 70 c has become significantly brighter in Hα between 2023 March and 2024 May. The observed variability suggests dynamic accretion processes, possibly modulated by circumplanetary disk properties or transient accretion bursts. High-amplitude variability in PDS 70 c motivates simultaneous monitoring of multiple accretion tracers to probe the mechanisms of mass growth of gas giant planets. We quantify the impact of variability on the detectability of protoplanets in imaging surveys and emphasize the need for continued and regular monitoring to accurately assess the occurrence and characteristics of young, forming planets.

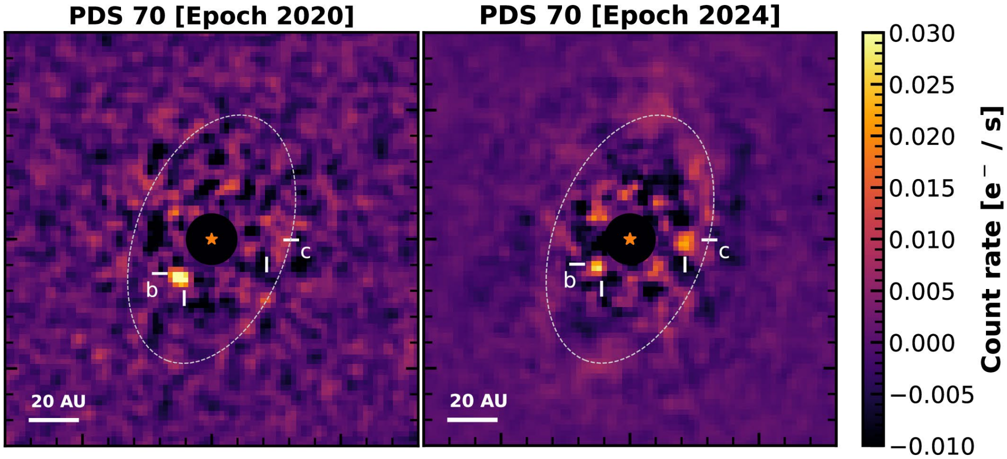

***Figure 1**. Primary-subtracted images of PDS 70 in 2020 (left) and 2024 (right). North is up and east is to the left. Color scales of the two panels are identical. The expected positions of PDS 70 b and c are marked. The white dashed line marks the inner edge of PDS 70's outer disk in infrared scattered light. PDS 70 b is detected in both epochs and demonstrates a significant orbital motion. PDS 70 c is only detected in Epoch 2024. The apparent brightness variations in PDS 70 b and c do not accurately represent the planets' intrinsic variability, as high-contrast imaging postprocessing introduces flux loss. For a comprehensive analysis of the evidence for variability, refer to Section 3.3.*

Three-dimensional Transport of Solids in a Protoplanetary Disk Containing a Growing Giant Planet

Van Clepper, Eric; Price, Ellen M.; Ciesla, Fred J.

The Astrophysical Journal, Volume 980, Issue 2, id.201, 15 pp.

We present the results of combined hydrodynamic and particle tracking post-processing modeling to study the transport of small dust in a protoplanetary disk containing an embedded embryo in three dimensions. We use a suite of FARGO3D hydrodynamic simulations of disks containing a planetary embryo varying in mass up to 300 $M_\oplus$ on a fixed orbit in both high- and low-viscosity disks. We then simulate solid particles through the disk as a post-processing step using a Monte Carlo integration, allowing us to track the trajectories of individual particles as they travel throughout the disk. We find that gas advection onto the planet can carry small, well-coupled solids across the gap opened in the disk by the embedded planet for planetary masses above the pebble isolation mass. This mixing between the inner and outer disk can occur in both directions, with solids in the inner disk mixing to the outer disk as well. Additionally, in low-viscosity disks, multiple dust pile-ups in the outer disk may preserve isotopic heterogeneities, possibly providing an outermost tertiary isotopic reservoir. Throughout Jupiter's growth, the extent of mixing between isotopic reservoirs varied depending on dust size, gas turbulence, and the Jovian embryo mass.

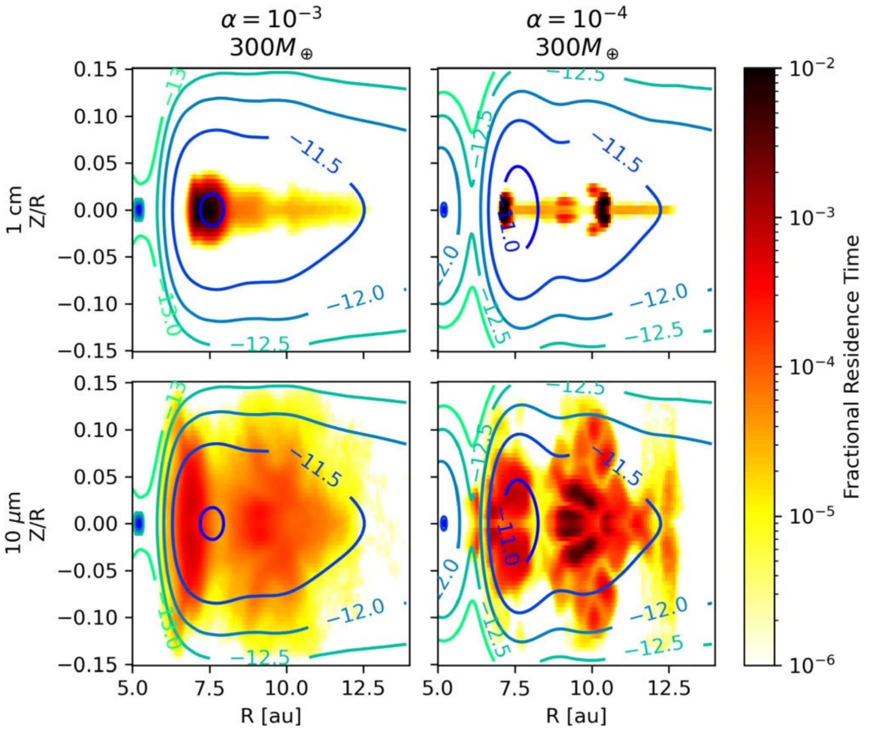

***Figure 13**. Azimuthally averaged residence times for the largest (top) and smallest (bottom) solids considered in high-viscosity (left) and low-viscosity (right) disks containing a 300 $M_\oplus$ planet. The contour lines show the surrounding gas density and are placed logarithmically, with contour labels indicating the log10 of the gas density. In the high-viscosity case, the solids diffuse more vertically and tend to concentrate near the gap. In the low-viscosity case, solids much more closely follow the gas advection, and are concentrated in much smaller areas. The small solids can spend significant amounts of time away from the midplane.*

The Doubly Librating Plutinos

Malhotra, Renu; Ito, Takashi

➔ The Astrophysical Journal, Volume 980, Issue 1, id.115, 6 pp.

Named for orbital kinship with Pluto, the Plutinos are a prominent group of Kuiper Belt objects whose orbital periods are in libration about a 3/2 ratio with Neptune's. We investigate the long-term orbital dynamics of known Plutinos, with attention to the additional libration (or lack thereof) of their argument of perihelion, g, a well-known characteristic of Pluto's orbit. We show that the g librators among the Plutinos cluster around an arc in the eccentricity–inclination parameter plane. This previously unreported dynamical structure is owed to a family of periodic orbits of the third kind in the restricted problem of three bodies, identified by Poincaré at the end of the 19th century. Approximately 16% of the currently known Plutinos exhibit g librations, a far greater fraction than the ratios of the associated libration frequencies. These results may offer new constraints for theoretical models of the dynamical history of the Plutinos and of the orbital migration history of the giant planets.

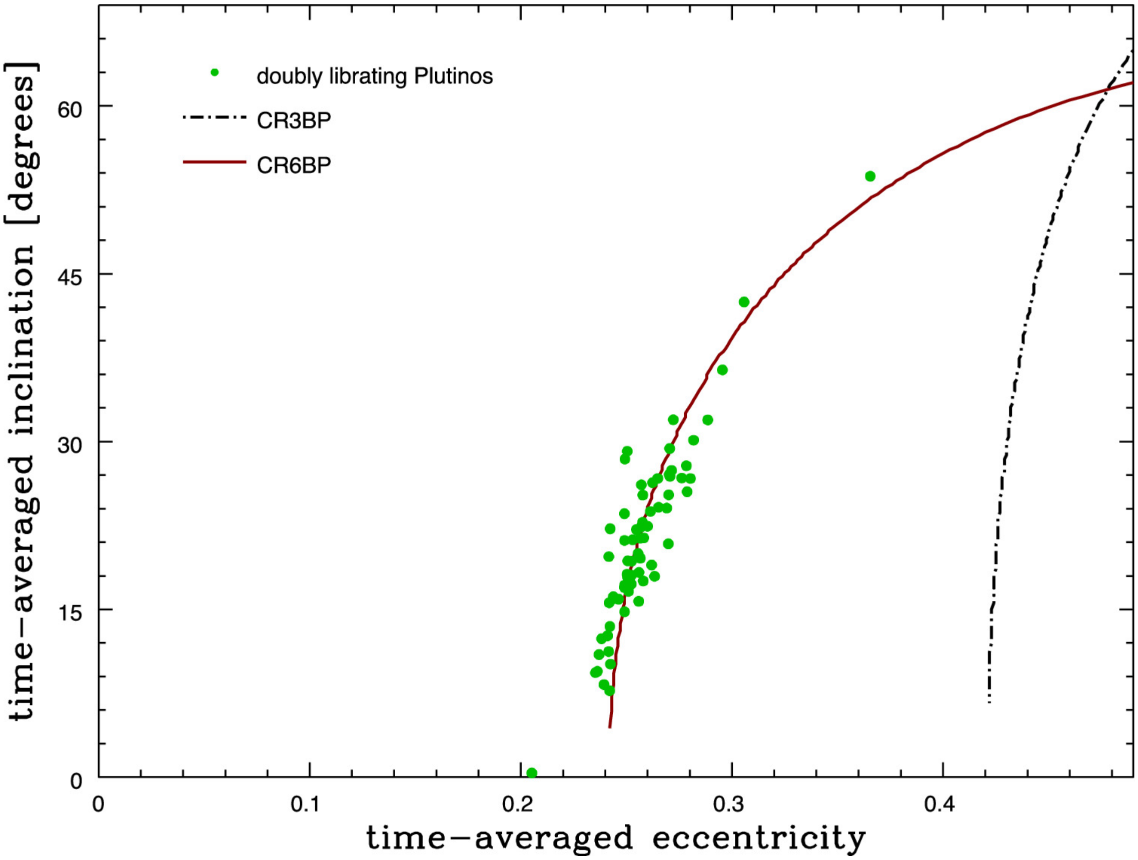

***Figure 3**. The doubly librating Plutinos (green dots), and the locus of the g libration centers of Plutinos in two models: the red curve was computed for the circular restricted six-body problem (CR6BP) of the Sun, the four giant planets and a (massless) Plutino, whereas the black dotted–dashed curve was computed for the circular restricted three-body problem (CR3BP) of the Sun, Neptune, and a (massless) Plutino. For both models we averaged over the mean longitudes, while taking account of the mean motion resonance constraints, to find the location of the minima of the disturbing function.*

Tides on Lava Worlds: Application to Close-in Exoplanets and the Early Earth–Moon System

Farhat, Mohammad; Auclair-Desrotour, Pierre; Boué, Gwenaël; Lichtenberg, Tim; Laskar, Jacques

The Astrophysical Journal, Volume 979, Issue 2, id.133, 24 pp.

Understanding the physics of planetary magma oceans has been the subject of growing efforts, in light of the increasing abundance of solar system samples and extrasolar surveys. A rocky planet harboring such an ocean is likely to interact tidally with its host star, planetary companions, or satellites. To date, however, models of the tidal response and heat generation of magma oceans have been restricted to the framework of weakly viscous solids, ignoring the dynamical fluid behavior of the ocean beyond a critical melt fraction. Here we provide a handy analytical model that accommodates this phase transition, allowing for a physical estimation of the tidal response of lava worlds. We apply the model in two settings: the tidal history of the early Earth–Moon system in the aftermath of the giant impact, and the tidal interplay between short-period exoplanets and their host stars. For the former, we show that the fluid behavior of the Earth's molten surface drives efficient early lunar recession to ~25 Earth radii within 104–105 yr, in contrast with earlier predictions. For close-in exoplanets, we report on how their molten surfaces significantly change their spin–orbit dynamics, allowing them to evade spin–orbit resonances and accelerating their track toward tidal synchronization from a gigayear to megayear timescale. Moreover, we reevaluate the energy budgets of detected close-in exoplanets, highlighting how the surface thermodynamics of these planets are likely controlled by enhanced, fluid-driven tidal heating, rather than vigorous insolation, and how this regime change substantially alters predictions for their surface temperatures.

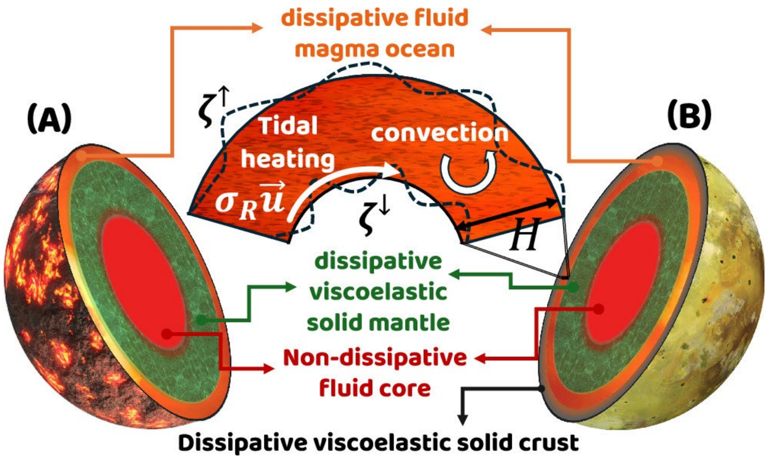

Figure 1. *A schematic illustrating the different planetary models under study. In both models, (A) and (B), the planet has a molten core that contributes negligibly to the tidally dissipated energy (this also stands if the core is differentiated into a solid inner and fluid outer parts). On top of the core lies a viscoelastic solid mantle which can be stratified and further divided into layers of uniform physical properties. Tidal dissipation in this mantle is computed in the solid tidal formalism using ALMA3 (Section 2.1). The solid mantle is enveloped by a fluid magma ocean of unperturbed uniform thickness H, which is the focus of our study. Under tidal forcing of the ocean and the mantle, the ocean's bottom (top) is displaced vertically by* $\zeta^{\downarrow}$ *(*$\zeta^{\uparrow}$*). This forcing also leads to heating (by virtue of several dissipative mechanisms in reality, but mainly due to friction at the ocean–solid mantle interface, as shown in the sketch). The heating is counteracted by convective cooling. This molten layer can either be the outermost layer of the planet (A), or it can live under a solidified crust (B).*

Discovery and Characterization of an Eccentric, Warm Saturn Transiting the Solar Analog TOI-4994

Rodríguez Martínez, Romy; Eastman, Jason D.; Collins, Karen A.; Rodriguez, Joseph E.; Charbonneau, David; Quinn, Samuel N.; Latham, David W.; Ziegler, Carl; Brahm, Rafael; Fairnington, Tyler R.; Ulmer-Moll, SolÉne; Stassun, Keivan G.; Suarez, Olga; Guillot, Tristan; Hobson, Melissa J.; Winn, Joshua N.; Kanodia, Shubham; Schlecker, Martin; Butler, R. P.; Crane, Jeffrey D.; Shectman, Steve; Teske, Johanna K.; Osip, David; Beletsky, Yuri ; Battley, Matthew P.; Psaridi, Angelica; Figueira, Pedro; Lendl, Monika; Bouchy, François ; Udry, Stéphane ; Kunimoto, Michelle; Mékarnia, Djamel ; Abe, Lyu ; Trifonov, Trifon; Tala Pinto, Marcelo ; Eberhardt, Jan; Espinoza, Nestor; Henning, Thomas; Jordán, Andrés; Rojas, Felipe I.; Barkaoui, Khalid; Relles, Howard M.; Srdoc, Gregor ; Collins, Kevin I.; Seager, Sara; Shporer, Avi; Vezie, Michael ; Hedges, Christina ; Mireles, Ismael

➔ The Astronomical Journal, Volume 169, Issue 2, id.72, 12 pp.

We present the detection and characterization of TOI-4994b (TIC 277128619b), a warm Saturn-sized planet discovered by the NASA Transiting Exoplanet Survey Satellite. TOI-4994b transits a G-type star (V = 12.6 mag) with a mass, radius, and effective temperature of , , and Teff = 5640 ± 110 K. We obtained follow-up ground-based photometry from the Las Cumbres Observatory and the Antarctic Search for Transiting ExoPlanets telescopes, and we confirmed the planetary nature of TOI-4994b with multiple radial velocity observations from the Planet Finder Spectrograph, CHIRON, High Accuracy Radial velocity Planet Searcher, Fiber-fed Extended Range Optical Spectrograph, and CORALIE instruments. From a global fit to the photometry and radial velocities, we determine that TOI-4994b is in a 21.5 day eccentric orbit (e = 0.32 ± 0.04) and has a mass of , a radius of , and a Saturn-like bulk density of . We find that TOI-4994 is a potentially viable candidate for follow-up stellar obliquity measurements. TOI-4994b joins the small sample of warm Saturn analogs and thus sheds light on our understanding of these rare and unique worlds. *This paper includes data gathered with the 6.5 m Magellan Telescopes located at Las Campanas Observatory, Chile.

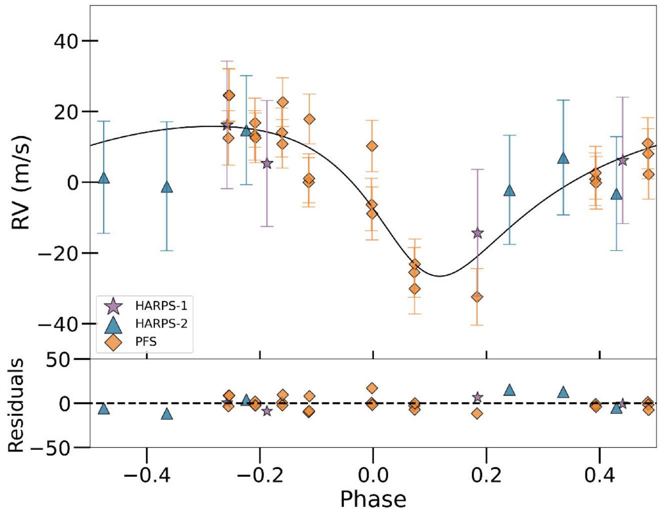

Figure 5*. Phase-folded radial velocities from PFS (golden diamonds) and HARPS (purple stars and blue triangles) only, with residuals plotted below.*

Three warm Jupiters orbiting TOI-6628, TOI-3837, and TOI-5027 and one sub-Saturn orbiting TOI-2328

Tala Pinto, Marcelo; Jordán, Andrés ; Acuña, Lorena; Jones, Matías ; Brahm, Rafael ; Reinarz, Yared; Eberhardt, Jan ; Espinoza, Néstor ; Henning, Thomas ; Hobson, Melissa ; Rojas, Felipe ; Schlecker, Martin ; Trifonov, Trifon ; Bakos, Gaspar; Boyle, Gavin; Csubry, Zoltan ; Hartmann, Joel ; Knepper, Benjamin; Kreidberg, Laura ; Suc, Vincent; Teske, Johanna; Butler, Robert Paul; Crane, Jeffrey; Schectman, Steve ; Thompson, Ian ; Osip, Dave ; Ricker, George ; Collins, Karen A. ; Watkins, Cristilyn N.; Bieryla, Allyson ; Stockdale, Chris; Wang, Gavin ; Zambelli, Roberto; Seager, Sara; Winn, Joshua ; Rose, Mark E.; Rice, Malena; Essack, Zahra

Astronomy & Astrophysics, Volume 694, id.A268, 19 pp.

We report the discovery and characterization of three new transiting giant planets orbiting TOI-6628, TOI-3837, and TOI-5027 and one new warm sub-Saturn orbiting TOI-2328, whose transits events were detected in the light curves of the Transiting Exoplanet Survey Satellite (TESS) space mission. By combining TESS light curves with ground-based photometric and spectroscopic followup observations, we confirm the planetary nature of the observed transits and radial velocity variations. TOI-6628 b has a mass of 0.74±0.06 MJ and a radius of 0.98-0.05+0.06 RJ and orbits a metal-rich star with a period of 18.18424 ± 0.00001 days and an eccentricity of 0.670-0.016+0.015, making it one of the most eccentric orbits of all known warm giants. TOI-3837 b has a mass of 0.59±0.05 MJ and a radius of 0.97-0.06+0.05 RJ and orbits its host star every 11.88865 ± 0.00003 days, with a moderate eccentricity of 0.221-0.046+0.042. With a mass of 2.02±0.13 MJ and a radius of 0.96-0.06+0.05 RJ, TOI-5027 b orbits its host star in an eccentric orbit with e = 0.385-0.026+0.025 every 10.24368±0.00001 days. TOI-2328 b is a Saturn-like planet with a mass of 0.16±0.02 MJ and a radius of 0.89-0.05+0.04 RJ; it orbits its host star in a nearly circular orbit with e = 0.057-0.029+0.046 at a period of 17.10197±0.00001 days. All four planets have orbital periods above ten days, and our planet's interior structure models are consistent with a rocky-icy core with an H/He envelope, providing evidence supporting the core-accretion model of planet formation for this kind of planet.

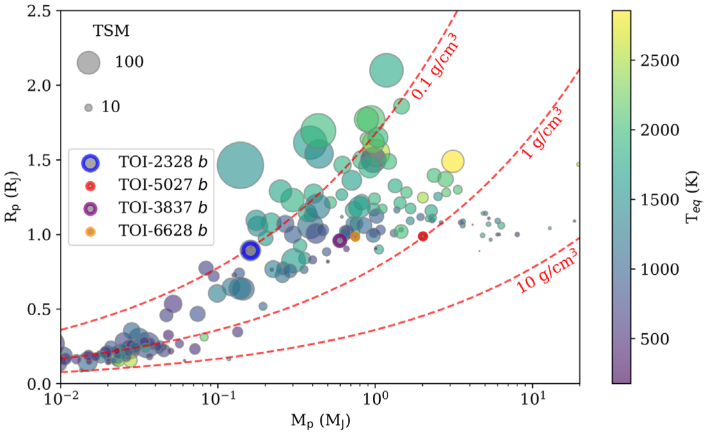

***Figure 11**. Planet radius as a function of the planet mass for the population of warm giant planets (P > 10 days), color-coded by equilibrium temperature. The size of the circles scales with the transit spectroscopy metric (TSM; Kempton et al. 2018). Dashed red lines correspond to bulk densities of 0.1, 1, and 10 g cm^{-3}.*

Characterization of seven transiting systems, including four warm Jupiters from SOPHIE and TESS

Heidari, N.; Hébrard, G. ; Martioli, E.; Eastman, J. D.; Jackson, J. M.; Delfosse, X. ; Jordán, A. ; Correia, A. C. M.; Sousa, S.; Dragomir, D.; Forveille, T.; Boisse, I. ; Giacalone, S. A. ; Díaz, R. F. ; Brahm, R. ; Almasian, D. ; Almenara, J. M. ; Bieryla, A. ; Barkaoui, K.; Baker, D.; Barros, S. C. C.; Bonfils, X. ; Carmona, A.; Collins, K. A. ; Cortés-Zuleta, P.; Deleuil, M.; Demangeon, O. D. S.; Edwards, B.; Eberhardt, J. ; Espinoza, N. ; Eisner, N. ; Feliz, D. L.; Frommer, A. C.; Fukui, A.; Grau, F.; Gupta, A. F. ; Hara, N. ; Hobson, M. J. ; Henning, T. ; Howell, S. B. ; Jenkins, J. M. ; Kiefer, F. ; LaCourse, D. M. ; Laskar, J. ; Law, N. ; Mann, A. W.; Murgas, F.; Moutou, C. ; Narita, N.; Palle, E.; Relles, H. M.; Stassun, K. G.; Serrano Bell, J.; Schwarz, R. P.; Srdoc, G. ; Strøm, P. A.; Safonov, B. ; Sarkis, P. ; Schlecker, M. ; Tala Pinto, M. ; Pepper, J. ; Rojas, F. I. ; Twicken, J. D. ; Trifonov, T. ; Villanueva, S. ; Watkins, C. N.; Winn, J. N. ; Ziegler, C.

➔ Astronomy & Astrophysics, Volume 694, id.A36, 31 pp.

While several thousand exoplanets are now confirmed, the number of known transiting warm Jupiters (10 d <period < 200 d) remains relatively small. These planets are generally believed to have formed outside the snowline and migrated to their current orbits. Because they are sufficiently distant from their host stars, they mitigate proximity effects and so offer valuable insights into planet formation and evolution. Here, we present the study of seven systems, three of which – TOI-2295, TOI-2537, and TOI-5110 – are newly discovered planetary systems. Through the analysis of TESS photometry, SOPHIE radial velocities (RVs), and high-spatial resolution imaging, we found that TOI-2295b, TOI-2537b, and TOI-5110b are transiting warm Jupiters with orbital periods ranging from 30 to 94 d, masses between 0.9 and 2.9 MJ, and radii ranging from 1.0 to 1.5 RJ. Both TOI-2295 and TOI-2537 harbor at least one additional, outer planet. Their outer planets – TOI-2295c and TOI-2537c – are characterized by orbital periods of 966.5-4.2+4.3 and 1920-140+230 d, respectively, and minimum masses of 5.61-0.24+0.23 and 7.23-0.45+0.52 MJ, respectively. We have also investigated and characterized the two recently reported warm Jupiters TOI-1836b and TOI-5076b, which we independently detected in SOPHIE RVs. Our new data allow for further discussion of their nature and refinement of their parameters. Additionally, we study the planetary candidates TOI-4081.01 and TOI-4168.01. [trunc.]

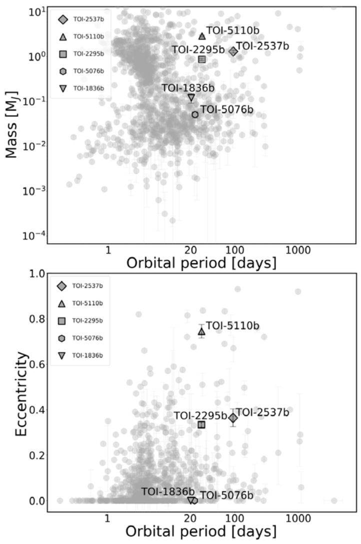

Figure 15*. Mass-period (top) and eccentricity-period (bottom) diagrams of characterized transiting planet in this study together with other exoplanets with known mass and radius from the NASA Exoplanet Data Archive (as of February 26, 2024). The bottom panel highlights the unique position of TOI-5110b as one of the most eccentric planets known to date.*

Super-Earths and Earth-like Exoplanets

Lichtenberg, Tim ; Miguel, Yamila

Treatise on Geochemistry (Third Edition), Volume 7, 2025, Pages 51-112

In the last few years astronomical surveys have expanded the reach of planetary science into the realm of small and dense extrasolar worlds. These share a number of characteristics with the terrestrial and icy planetary objects of the Solar System, but keep stretching previous understanding of the known limits of planetary thermodynamics, material properties, and climate regimes. Improved compositional and thermal constraints on exoplanets below ~

2 Earth radii suggest efficient accretion of atmosphere-forming volatile elements in a fraction of planetary systems, pointing to rapid formation, planet-scale melting, and chemical equilibration between the core, mantle, and atmosphere of rocky and volatile-rich exoplanets. Meaningful interpretation of novel observational data from these worlds necessitates cross-disciplinary expansion of known material properties under extreme thermodynamic, non-solar conditions, and accounting for dynamic feedbacks between interior and atmospheric processes. Exploration of the atmosphere and surface composition of individual, short-period super-Earths in the next few years will enable key inferences on magma ocean dynamics, the redox state of rocky planetary mantles, and mixing between volatile and refractory phases in planetary regimes that are absent from the present-day Solar System, and reminiscent of the conditions of the prebiotic Earth. The atmospheric characterization of climate diversity and the statistical search for biosignatures on terrestrial exoplanets on temperate orbits will require space-based direct imaging surveys, capable of resolving emission features of major and trace gases in both shortwave and mid-infrared wavelengths.

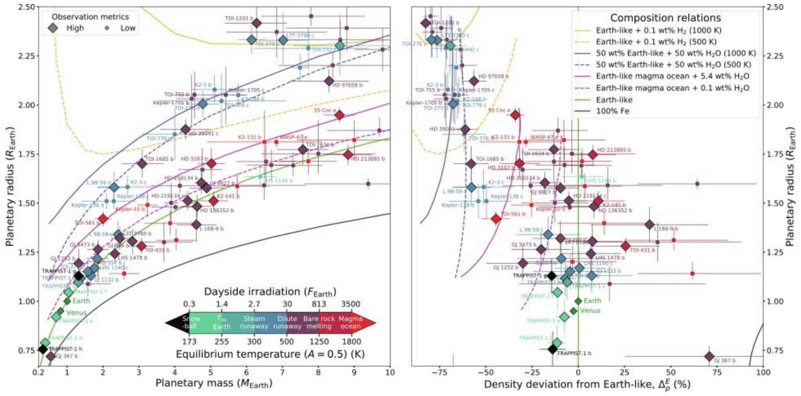

Figure 6. *(Left) Measured exoplanet radii as a function of mass relative to idealized composition curves. (Right) Radii vs density deviation relative to Earth-like. Colored symbols represent the best-characterized exoplanets with mass uncertainties below 50% and radius uncertainties below 30%. Data points from Otegi et al. (2020), Lacedelli et al. (2022), Luque and Pallé (2022), Diamond-Lowe et al. (2022), and Piaulet et al. (2023). Mass–radius relations from Zeng et al. (2019) and Dorn and Lichtenberg (2021). Diamond symbols with attached names indicate planets with high transmission (TSM) or emission (ESM) metrics, which makes these planets favorable targets for observational characterization: TSM > 90 if $R_p \geq 1.5R_{Earth}$, otherwise TSM > 10, or ESM > 7.5 (Kempton et al., 2018). The translation of dayside irradiation to equilibrium temperature assumes efficient global heat redistribution and a constant bond albedo of 0.5. Color deviations and trend interpretation are discussed in the main text.*

History and Habitability of the LP 890-9 Planetary System

Barnes, Rory; do Amaral, Laura N. R.; Birky, Jessica; Carone, Ludmila; Driscoll, Peter ; Livesey, Joseph R.; Graham, David ; Becker, Juliette; Cui, Kaiming; Schlecker, Martin; Garcia, Rodolfo ; Gialluca, Megan; Adams, Arthur; Ahmed, MD Redyan; Bonney, Paul; Broussard, Wynter; Chawla, Chetan; Damasso, Mario; Danchi, William C.; Deitrick, Russell; Ducrot, Elsa; Fromont, Emeline F.; Gaches, Brandt A. L.; Gupta, Sakshi; Hill, Michelle L.; Jackman, James A. G. ; Janin, Estelle M.; Karawacki, Mikołaj; Koren, Matheus Daniel; La Greca, Roberto ; Leung, Michaela; Miranda-Rosete, Arturo; Olohoy, Michael Kent A.; Ngo, Cecelia ; Paul, Daria; Sahu, Chandan Kumar; Sarkar, Debajyoti Basu; Shadab, Mohammad Afzal; Schwieterman, Edward W.; Sedler, Melissa ; Texeira, Katie ; Vazan, Allona; Delgado Vega, Karen N. ; Vijayakumar, Rohit; Wojack, Jonathan T.

The Planetary Science Journal, Volume 6, Issue 1, id.25, 13 pp.

We present numerous aspects of the evolution of the LP 890-9 (SPECULOOS-2/TOI-4306) planetary system, focusing on the likelihood that planet c can support life. We find that the host star reaches the main sequence in 1 Gyr and that planet c lies close to the inner boundary of the habitable zone. We find the magma ocean stage can last up to 50 Myr, remove eight Earth oceans of water, and leave up to 2000 bars of oxygen in the atmosphere. However, if the planet forms with a hydrogen envelope as small as 0.1 Earth masses, no water will be lost during the star's pre-main-sequence phase from thermal escape processes. We find that the planets are unlikely to be in a 3:1 mean motion resonance and that both planets tidally circularize within 0.5 Gyr when tidal dissipation is held constant. However, if tidal dissipation is a function of mantle temperature and rheology, then we find that planet c's orbit may require more than 7 Gyr to circularize, during which time tidal heating may reach hundreds of terawatts. We thus conclude that the habitability of planet c depends most strongly on the initial volatile content and internal properties, but no data yet preclude the viability of an active biosphere on the planet.

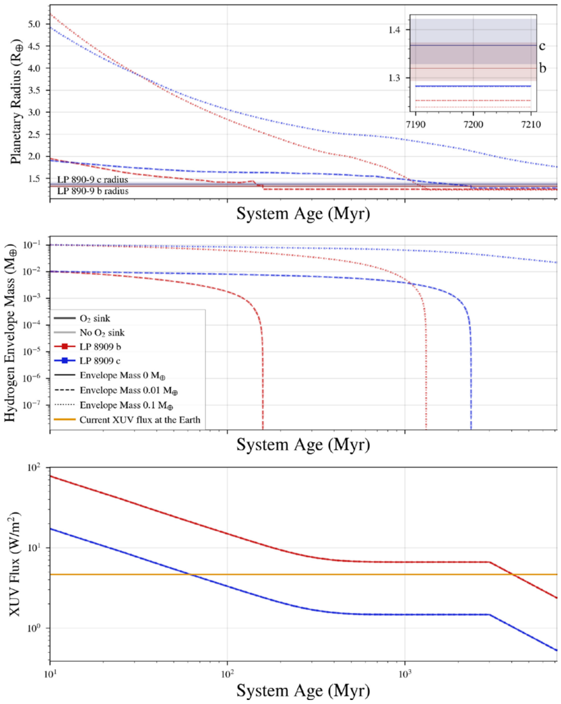

Figure 4. Time evolution of planetary radius (upper panel), hydrogen envelope mass (middle panel), and XUV flux at the planetary atmosphere (bottom panel). The horizontal orange line in the bottom panel indicates the XUV flux on the present Earth. Horizontal lines in the top panel indicate the observed planetary radii of LP 890-9 b and c (L. Delrez et al. 2022). The shadow in the inset of the top panel shows the planetary radius uncertainty.

Convective shutdown in the atmospheres of lava worlds

Nicholls, Harrison; Pierrehumbert, Raymond T. ; Lichtenberg, Tim; Soucasse, Laurent ; Smeets, Stef

Monthly Notices of the Royal Astronomical Society, Volume 536, Issue 3, pp.2957-2971

Atmospheric energy transport is central to the cooling of primordial magma oceans. Theoretical studies of atmospheres on lava planets have assumed that convection is the only process involved in setting the atmospheric temperature structure. This significantly influences the ability for a magma ocean to cool. It has been suggested that convective stability in these atmospheres could preclude permanent magma oceans. We develop a new 1D radiative-convective model in order to investigate when the atmospheres overlying magma oceans are convectively stable. Using a coupled interior-atmosphere framework, we simulate the early evolution of two terrestrial-mass exoplanets: TRAPPIST-1 c and HD 63433 d. Our simulations suggest that the atmosphere of HD 63433 d exhibits deep isothermal layers which are convectively stable. However, it is able to maintain a permanent magma ocean and an atmosphere depleted in H2O. It is possible to maintain permanent magma oceans underneath atmospheres without convection. Absorption features of CO2 and SO2 within synthetic emission spectra are associated with mantle redox state, meaning that future observations of HD 63433 d may provide constraints on the geochemical properties of a magma ocean analogous with the early Earth. Simulations of TRAPPIST-1 c indicate that it is expected to have solidified within 100Myr, outgassing a thick atmosphere in the process. Cool isothermal stratospheres generated by low-molecular-weight atmospheres can mimic the emission of an atmosphere-less body. Future work should consider how atmospheric escape and chemistry modulates the lifetime of magma oceans, and the role of tidal heating in sustaining atmospheric convection.

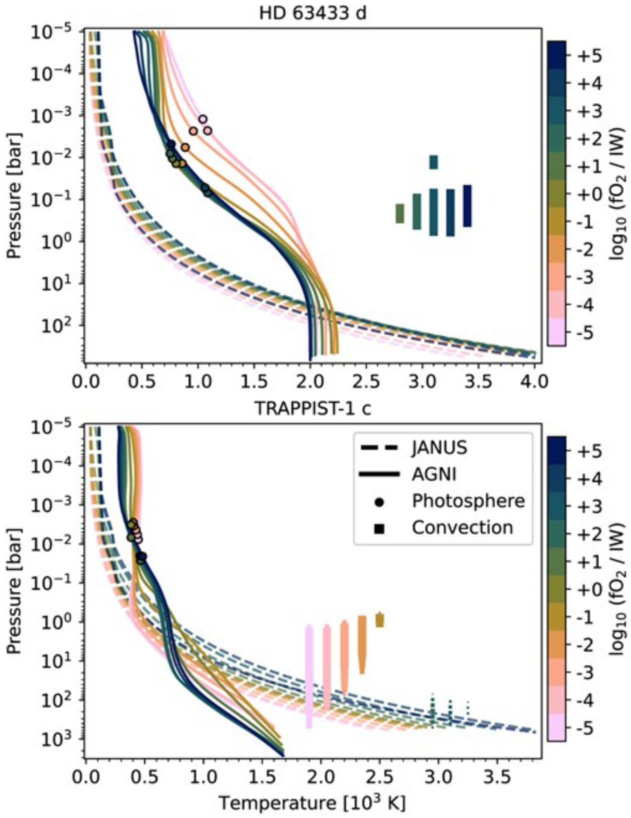

***Figure 5**. Atmospheric temperature profiles at model termination for HD 63 433 d (top) and TRAPPIST-1 c (bottom), versus mantle fO_2 (line colour), simulated with both atmosphere models (line style). Square markers denote the presence of convective regions in the agni cases, where the marker sizes scale with the relative amount of the total flux at each pressure level that is carried by convection; the horizontal positioning of these markers is for visualization purposes. At the full square marker size (legend entry), convection is responsible for all upward flux transport at that level. Circular markers denote the effective photospheres, taken to be the pressure levels at which the contribution functions are maximized in each case (Knutson et al. 2009; Drummond et al. 2016; Boukrouche et al. 2021). Note the different axis limits between the subplots.*

Stellar Contamination Correction Using Back-to-back Transits of TRAPPIST-1 b and c

Rathcke, Alexander D.; Buchhave, Lars A.; de Wit, Julien; Rackham, Benjamin V.; August, Prune C.; Diamond-Lowe, Hannah; MendonÇa, João M.; Bello-Arufe, Aaron; López-Morales, Mercedes; Kitzmann, Daniel; Heng, Kevin

➔ The Astrophysical Journal Letters, Volume 979, Issue 1, id.L19, 10 pp.

Stellar surface heterogeneities, such as spots and faculae, often contaminate exoplanet transit spectra, hindering precise atmospheric characterization. We demonstrate a novel, epoch-based, model-independent method to mitigate stellar contamination, applicable to multiplanet systems with at least one airless planet. We apply this method using quasi-simultaneous transits of TRAPPIST-1 b and TRAPPIST-1 c observed on 2024 July 9, with JWST/NIRSpec PRISM. These two planets, with nearly identical radii and impact parameters, are likely to either be bare rocks or possess thin, low-pressure atmospheres, making them ideal candidates for this technique, as variations in their transit spectra would be primarily attributed to stellar activity. Our observations reveal their transit spectra exhibit consistent features, indicating similar levels of stellar contamination. We use TRAPPIST-1 b to correct the transit spectrum of TRAPPIST-1 c, achieving a 2.5 × reduction in stellar contamination at shorter wavelengths. At longer wavelengths, lower signal-to-noise ratio prevents clear detection of contamination or full assessment of mitigation. Still, out-of-transit analysis reveals variations across the spectrum, suggesting contamination extends into the longer wavelengths. Based on the success of the correction at shorter wavelengths, we argue that contamination is also reduced at longer wavelengths to a similar extent. This shifts the challenge of detecting atmospheric features to a predominantly white noise issue, which can be addressed by stacking observations. This method enables epoch-specific stellar contamination corrections, allowing coaddition of planetary spectra for reliable searches of secondary atmospheres with signals of 60–250 ppm. Additionally, we identify small-scale cold (∼2000 K) and warm (∼2600 K) regions almost uniformly distributed on TRAPPIST-1, with overall covering fractions varying by ∼0.1% per hour.

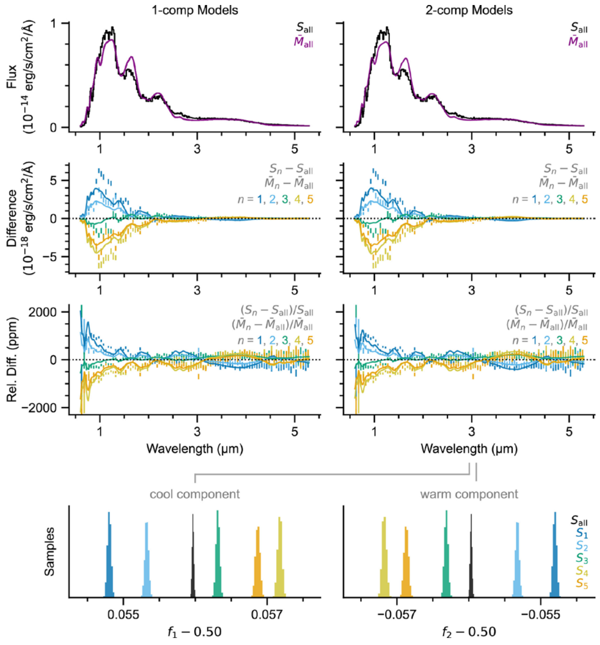

Figure 2. *Out-of-transit stellar spectra and model fits. Top row: mean stellar spectrum for all out-of-transit data (S_{all}, which combines the S_1 through S_5 stellar spectra, as defined by the out-of-transit segments shown in Figure 1) alongside the 1-component (left) and 2-component (right) model fits (M¯all). Both fits are qualitatively similar, as are the more complex models we tested. Second row: observed spectra (S_1 to S_5), shown as differences relative to S_{all} (colored points, binned in wavelengths for visual clarity), and model fits (M¯1 to M¯5) relative to M¯all (solid colored lines). Third row: same as the second row, but normalized at each wavelength to highlight relative changes. Bottom row: histograms of the posterior sample distributions for covering fractions in the 2-component fits. While the temperatures do not vary with time, the posterior estimates of the covering fractions evince a trend in which the covering fraction of the cool component (f_1) increases over the observations, reaching a maximum after the transits, and then decreases in the last time segment. This is consistent with the stellar brightness variations.*

Dynamics of Small, Constant-size Particles in a Protoplanetary Disk with an Embedded Protoplanet

Price, Ellen M.; Van Clepper, Eric; Ciesla, Fred J.

The Astrophysical Journal, Volume 979, Issue 1, id.37, 11 pp.

Hydrodynamical simulations of protoplanetary disk dynamics are useful tools for understanding the formation of planetary systems, including our own. Approximations are necessary to make these simulations computationally tractable. A common assumption when simulating dust fluids is that of a constant Stokes number, a dimensionless number that characterizes the interaction between a particle and the surrounding gas. Constant Stokes number is not a good approximation in regions of the disk where the gas density changes significantly, such as near a planet-induced gap. In this paper, we relax the assumption of a constant Stokes number in the popular FARGO3D code using semianalytic equations for the drag force on dust particles, which enables an assumption of constant particle size instead. We explore the effect this change has on disk morphology and particle fluxes across the gap for both outward- and inward-drifting particles. The assumption of constant particle size, rather than constant Stokes number, is shown to make a significant difference in some cases, emphasizing the importance of the more accurate treatment.

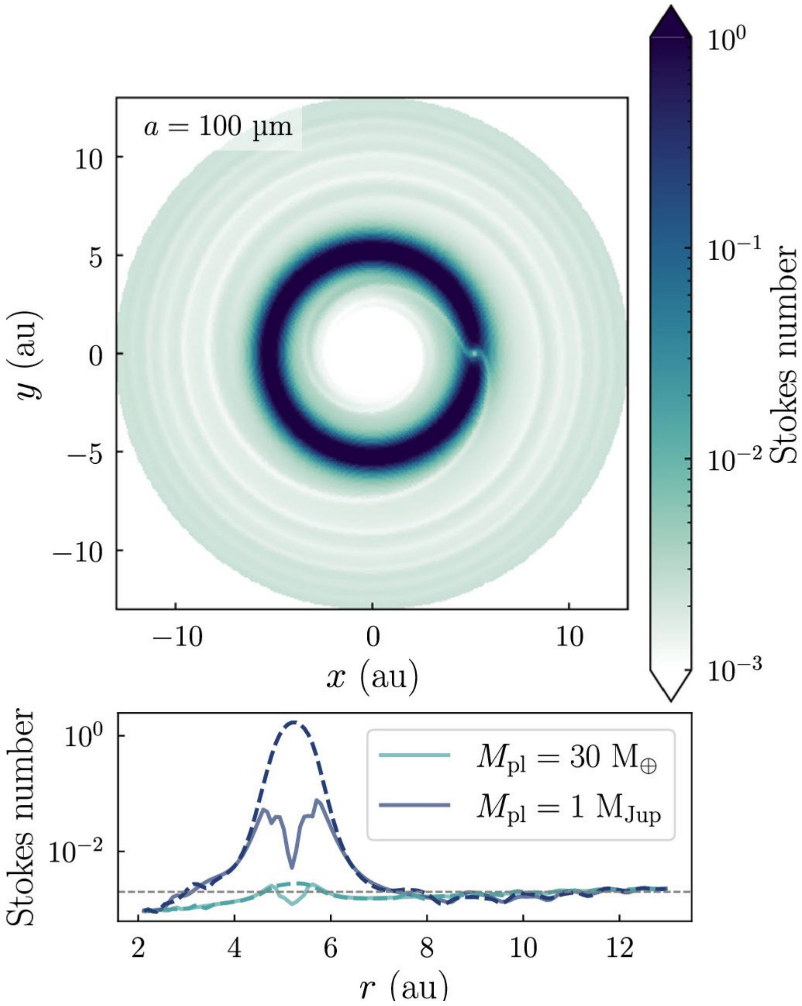

Figure 3. *In the upper panel, we show a map of the Stokes number computed for particles of constant size 100 µm in the presence of a Jupiter-mass planet, after evolution for 2000 orbits. In the lower panel, we show the Stokes number along negative x-axis (dashed) and positive x-axis (solid) for two different planet masses, indicating the corresponding assumed Stokes number with a dashed line. While the Stokes number increases dramatically inside the planet-induced gap compared to its surroundings, there is little to no material there to experience this level of decoupling from the gas. In the outer disk, we see that variations in the Stokes number are of order a few.*

Reliable Detections of Atmospheres on Rocky Exoplanets with Photometric JWST Phase Curves

Hammond, Mark; Guimond, Claire Marie; Lichtenberg, Tim; Nicholls, Harrison; Fisher, Chloe; Luque, Rafael; Meier, Tobias G.; Taylor, Jake; Changeat, Quentin; Dang, Lisa; Hay, Hamish C. F. C.; Herbort, Oliver; Teske, Johanna

The Astrophysical Journal Letters, Volume 978, Issue 2, id.L40, 17 pp.

The prevalence of atmospheres on rocky planets is one of the major questions in exoplanet astronomy, but there are currently no published unambiguous detections of atmospheres on any rocky exoplanets. The MIRI instrument on JWST can measure thermal emission from tidally locked rocky exoplanets orbiting small, cool stars. This emission is a function of their surface and atmospheric properties, potentially allowing detections of atmospheres. One way to find atmospheres is to search for lower dayside emission than would be expected for a blackbody planet. Another technique is to measure phase curves of thermal emission to search for nightside emission due to atmospheric heat redistribution. Here, we compare strategies for detecting atmospheres on rocky exoplanets. We simulate secondary eclipse and phase curve observations in the MIRI F1500W and F1280W filters for a range of surfaces (providing our open-access albedo data) and atmospheres on 30 exoplanets selected for their F1500W signal-to-noise ratio. We show that secondary eclipse observations are more degenerate between surfaces and atmospheres than suggested in previous work, and that thick atmospheres can support emission consistent with a blackbody planet in these filters. These results make it difficult to unambiguously detect or rule out atmospheres using their photometric dayside emission alone. We suggest that an F1500W phase curve could instead be observed for a similar sample of planets. While phase curves are time-consuming and their instrumental systematics can be challenging, we suggest that they allow the only unambiguous detections of atmospheres by nightside thermal emission.

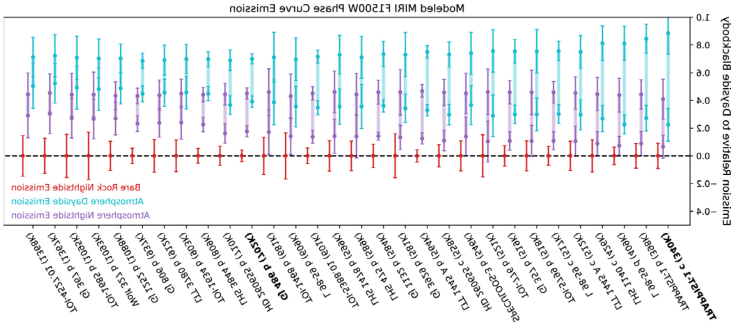

Figure 5. The ranges of modeled (and then fitted) F1500W phase curve maxima and minima for the range of atmospheres in Table 1 compared to the zero flux minimum expected on the nightside of a bare-rock planet. Each observation is modeled as a phase curve over one orbit. The plotted points are the true value of the maxima and minima of the phase curves, and the error bars are the 1σ uncertainty of the values fitted with J. Salvatier et al. (2016). As we did for the eclipse-only observations, the error bars are conservatively scaled up by 50% to ensure that they are at least as large as they would be for real observations. With a heat redistribution of 25% of the dayside energy to the nightside, almost every planet has detectable nightside emission. Those that do not are atmospheres with low CO2 abundances on planets with low signal-to-noise ratios; these also have detectably weak emission from their dayside as a result. We do not include the dayside emission for bare-rock surfaces, as these are shown in Figure 3 with comparable precision to that achieved by a phase curve. Moreover, our aim in the current figure is to identify unambiguous information by distinguishing nonzero nightside emission due to atmospheric heat redistribution.

TOI-4504: Exceptionally Large Transit Timing Variations Induced by Two Resonant Warm Gas Giants in a Three-planet System

Vítková, Michaela; Brahm, Rafael; Trifonov, Trifon; Kabáth, Petr; Jordán, Andrés; Henning, Thomas; Hobson, Melissa J.; Eberhardt, Jan; Pinto, Marcelo Tala; Rojas, Felipe I.; Espinoza, Nestor; Schlecker, Martin; Jones, Matías I. ; Moyano, Maximiliano; Eyheramendy, Susana; Ziegler, Carl; Lissauer, Jack J.; Vanderburg, Andrew; Collins, Karen A.; Wohler, Bill; Watanabe, David; Ricker, George R.; Vanderspek, Roland; Seager, Sara; Winn, Joshua N.; Jenkins, Jon M.; Skarka, Marek

➔ The Astrophysical Journal Letters, Volume 978, Issue 2, id.L22, 16 pp.

We present a joint analysis of transit timing variations (TTVs) and Doppler data for the transiting exoplanet system TOI-4504. TOI-4504 c is a warm Jupiter-mass planet that exhibits the largest known TTVs, with a peak-to-node amplitude of ∼2 days, the largest value ever observed, and a superperiod of ~930 days. TOI-4504 b and c were identified in public Transiting Exoplanet Survey Satellite (TESS) data, while the TTVs observed in TOI-4504 c, together with radial velocity (RV) data collected with FEROS, allowed us to uncover a third, nontransiting planet in this system, TOI-4504 d. We were able to detect transits of TOI-4504 b in the TESS data with a period of 2.4261 ± 0.0001 days and derive a radius of 2.69 ± 0.19 R⊕. The RV scatter of TOI-4504 was too large to constrain the mass of TOI-4504 b, but the RV signals of TOI-4504 c and d were sufficiently large to measure their masses. The TTV+RV dynamical model we apply confirms TOI-4504 c as a warm Jupiter planet with an osculating period of 82.54 ± 0.02 days, a mass of 3.77 ± 0.18 MJ, and a radius of 0.99 ± 0.05 RJ, while the nontransiting planet TOI-4504 d has an orbital period of 40.56 ± 0.04 days and a mass of 1.42 MJ. We present the discovery of a system with three exoplanets: a hot sub-Neptune and two warm Jupiter planets. The gas giant pair is stable and likely locked in a first-order 2:1 mean-motion resonance (MMR). The TOI-4504 system is an important addition to MMR pairs, whose increasing occurrence supports a smooth migration into a resonant configuration during the protoplanetary disk phase.

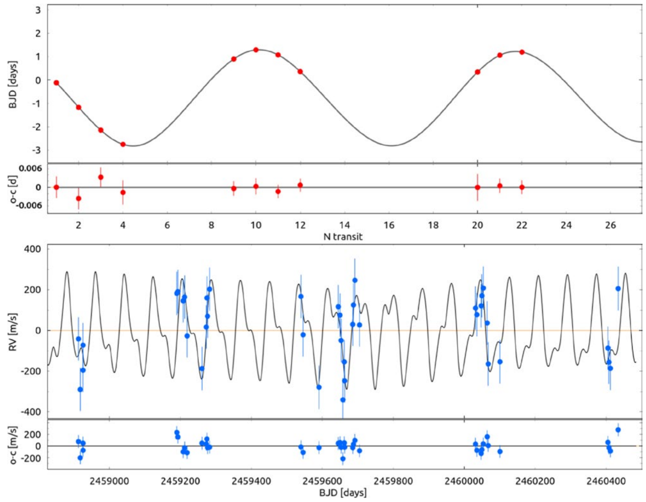

***Figure 6**. TESS TTV time series of TOI-4504 c and a model consistent with two Jovian-mass planets with periods close to the 2:1 MMR commensurability, with the nontransiting planet being interior (top panel). The TTV signal is expressed as the deviation of the TESS transit events with respect to the mean osculating period of TOI-4504 c, which has a large semiamplitude of ~2 days and a superperiod of 946.5 days. The bottom subpanel shows the TTV residuals. The main bottom panel shows the Doppler component of the same model fitted to the FEROS RV data. The bottom subpanel shows the RV residuals.*

JWST Captures a Sudden Stellar Outburst and Inner Disk Wall Destruction

Xie, Chengyan; Pascucci, Ilaria; Deng, Dingshan; Bajaj, Naman S.; Alexander, Richard; Sellek, Andrew; Kóspál, Ágnes; Ballabio, Giulia; Gorti, Uma

➔ The Astrophysical Journal, Volume 978, Issue 1, id.34, 12 pp.

We analyze JWST/MIRI observations of T Cha, a highly variable ($\Delta V \sim$ 3–5 mag) accreting Sun-like star surrounded by a disk with a large (~15 au) dust gap. We find that the JWST mid-IR spectrum is significantly different from the Spitzer spectrum obtained 17 yr before—the emission at short wavelengths (5–10 μm) has decreased by ~2/3 while that at longer wavelengths (15–25 μm) has increased by up to a factor of ~3. The JWST spectrum is contemporaneous with a fairly constant higher optical emission captured by the All Sky Automated Survey. After analyzing and modeling both spectral energy distributions, we propose that JWST caught the star during an outburst that partly destroyed and significantly reduced the height of the asymmetric inner disk wall responsible for the high optical variability and lower 15–25 μm emission during the Spitzer period. The dust mass lost during this outburst is estimated to be comparable (~1/5) to the upper limit of the total micron-sized dust mass in the inner disk of T Cha now. Monitoring this system during possible future outbursts and more observations of its quiescent state will reveal if the inner disk can be replenished or will continue to be depleted and vanish.

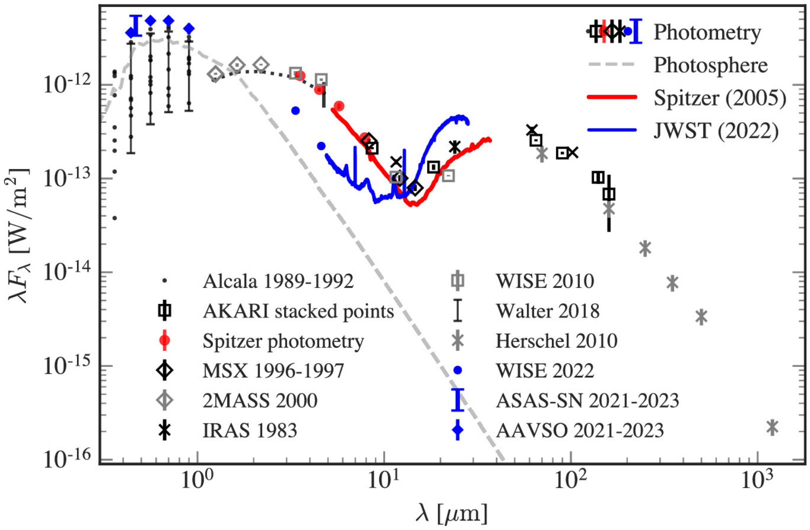

Figure 3*. Overview of the SED of T Cha. The gray dashed line is the 5600 K stellar photosphere emission scaled to the distance to T Cha. The red and blue solid lines are the Spitzer/IRS SED and JWST/MIRI-MRS spectra, respectively. The two strong lines in the JWST spectrum are [Ar II] and [Ne II], and the broad features are PAH features. The photometric points in optical bands are from J. M. Alcala et al. (1993), F. M. Walter et al. (2018), and AAVSO, and the IR photometric points are from various papers (see Table 5). We highlight some points in blue to indicate they were taken contemporaneously with the JWST observation (see the blue shaded region next to the JWST line in Figure 1). The NIR and mid-IR points connected with dotted lines indicate one contemporaneous observation at the JHKLM bands (J. M. Alcala et al. 1993). The photometry and spectra shown in this figure are available as Data behind the Figure.*

Three Years of High-contrast Imaging of the PDS 70 b and c Exoplanets at Hα with MagAO-X: Evidence of Strong Protoplanet Hα Variability and Circumplanetary Dust

Close, Laird M.; Males, Jared R.; Li, Jialin; Haffert, Sebastiaan Y.; Long, Joseph D.; Hedglen, Alexander D. ; Weinberger, Alycia J.; Follette, Katherine B.; Apai, Daniel; Doyon, Rene; Foster, Warren ; Gasho, Victor ; Van Gorkom, Kyle ; Guyon, Olivier; Kautz, Maggie Y.; Kueny, Jay; Lumbres, Jennifer ; McLeod, Avalon ; McEwen, Eden ; Pavao, Clarissa ; Pearce, Logan; Perez, Laura; Schatz, Lauren ; Szulágyi, Judit; Wagner, Kevin; Wu, Ya-Lin

➔ The Astronomical Journal, Volume 169, Issue 1, id.35, 29 pp.

We present 3 yr of high-contrast imaging of the PDS 70 b and c accreting protoplanets with the new extreme AO system MagAO-X as part of the MaxProtoPlanetS survey of Hα protoplanets. In 2023 and 2024, our sharp (25–27 mas FWHM), well-AO-corrected (20%–26% Strehl), deep (2–3.6 hr) images detected compact (r ~ 30 mas; r ~ 3 au) circumplanetary disks (CPDs) surrounding both protoplanets. Starlight scattering off the front edge of these dusty CPDs is the likely source of the bright compact continuum light detected within ~30 mas of both planets in our simultaneously obtained continuum 668 nm filter images. After subtraction of contaminating continuum and point-spread function residuals with pyKLIP angular differential imaging and spectral differential imaging, we obtained high-contrast ASDI Hα images of both planets in 2022, 2023, and 2024. We find the Hα line flux of planet b fell by (8.1 ± 1.6) × 10-16 erg s-1 cm-2, a factor of 4.6 drop in flux from 2022 to 2023. In 2024 March, planet b continued to be faint with just a slight 1.6× rise to an Hα line flux of (3.64 ± 0.87) × 10-16 erg s-1 cm-2. For c, we measure a significant increase of (2.74 ± 0.51) × 10-16 erg s-1 cm-2 from 2023 to 2024, which is a factor of 2.3 increase. So both protoplanets have recently experienced significant Hα variability with ~1 yr sampling. In 2024, planet c is brighter than b: as c is brightening and b generally fading. We also tentatively detect one new point source "CC3" inside the inner disk (~49 mas; at PA ~ 295° ; 2024) with orbital motion roughly consistent with a ~5.6 au orbit.

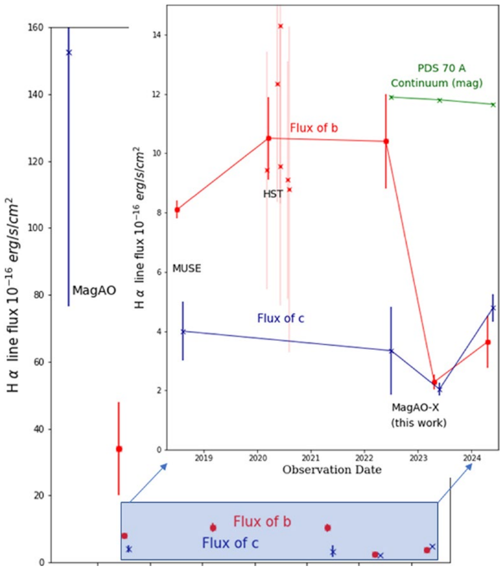

Figure 12.*The calculated Hα line fluxes of planets b and c, assuming no extinction ($A_R = A_p = 0$ mag) from the last two columns of Table 4. The main plot covers 7 yr of observations and has a large Y-axis upper limit to accommodate the 2017 February archival MagAO image recovery of c (K. B. Follette et al. 2023). Even though the errors are large, it appears that both c and b may have been much brighter at Hα around 6–7 yr ago. Then, from 2018 April to 2022 April, planet b was roughly constant at ~11 × 10^{-16} erg s^{-1} cm^{-2} (see inset for zoom in), but then from 2023 March onward, b dramatically faded to just ~2–3 × 10^{-16} erg s^{-1} cm^{-2}. Planet c's line flux has been roughly constant since 2018 April at ~5 × 10^{-16} erg s^{-1} cm^{-2}. Yet, we see evidence that c's flux is changing with a slight (but significant) 2.3× increase from 2023 to 2024. The green points are the magnitudes of PDS 70 A that we observed in the continuum filter and converted to r′. This variability of PDS 70 A in the continuum was accounted for and calibrated out of our MagAO-X line fluxes in this work. These data suggest that b is generally fading at Hα but c has recently brightened and now surpasses b.*

Magma Ocean Evolution at Arbitrary Redox State

Nicholls, Harrison; Lichtenberg, Tim; Bower, Dan J. ; Pierrehumbert, Raymond

Journal of Geophysical Research: Planets, Volume 129, Issue 12, page 2024JE008576, 28 pp.

Interactions between magma oceans and overlying atmospheres on young rocky planets leads to an evolving feedback of outgassing, greenhouse forcing, and mantle melt fraction. Previous studies have predominantly focused on the solidification of oxidized Earth-similar planets, but the diversity in mean density and irradiation observed in the low-mass exoplanet census motivate exploration of strongly varying geochemical scenarios. We aim to explore how variable redox properties alter the duration of magma ocean solidification, the equilibrium thermodynamic state, melt fraction of the mantle, and atmospheric composition. We develop a 1D coupled interior-atmosphere model that can simulate the time-evolution of lava planets. This is applied across a grid of fixed redox states, orbital separations, hydrogen endowments, and C/H ratios around a Sun-like star. The composition of these atmospheres is highly variable before and during solidification. The evolutionary path of an Earth-like planet at 1 AU ranges between permanent magma ocean states and solidification within 1 Myr. Recently solidified planets typically host H2O- or H2-dominated atmospheres in the absence of escape. Orbital separation is the primary factor determining magma ocean evolution, followed by the total hydrogen endowment, mantle oxygen fugacity, and finally the planet's C/H ratio. Collisional absorption by H2 induces a greenhouse effect which can prevent or stall magma ocean solidification. Through this effect, as well as the outgassing of other volatiles, geochemical properties exert significant control over the fate of magma oceans on rocky planets.

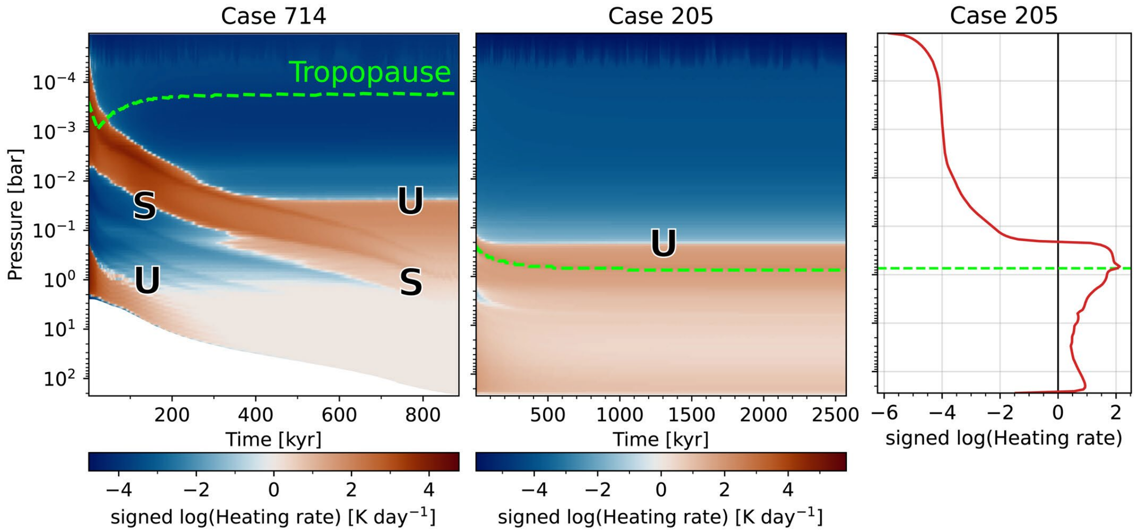

***Figure 10**. Radiative heating rate versus pressure and time. Case 714 (left) fully solidifies, and was discussed in Section **3.5**. Case 205 (center) reaches global radiative equilibrium while maintaining a significant melt fraction of 97.6% under a CO- and H2-dominated atmosphere. The dashed green lines indicate the tropopause. Regions of relative radiative heating and cooling are labeled “U” and “S,” corresponding to whether or not they are unstable or stable to convection. The rightmost panel plots the radiative heating profile at the final timestep of Case 205.*

Imaging of the Vega Debris System Using JWST/MIRI

Su, Kate Y. L.; Gáspár, András; Rieke, George H.; Malhotra, Renu; Matrá, Luca; Wolff, Schuyler Grace; Leisenring, Jarron M.; Beichman, Charles; Ygouf, Marie

The Astrophysical Journal, Volume 977, Issue 2, id.277, 23 pp.

We present images of the Vega planetary debris disk obtained at 15.5, 23, and 25.5 µm with the Mid-Infrared Instrument on JWST. The debris system is remarkably symmetric, smooth, and centered accurately on the star. There is a broad Kuiper-belt-analog ring at ~80–170 au that coincides with the planetesimal belt detected with the Atacama Large Millimeter/submillimeter Array at 1.34 mm. The interior of the broad belt is filled with warm debris that shines most efficiently at mid-infrared, along with a shallow flux dip/gap at 60 au from the star. These qualitative characteristics argue against any Saturn-mass planets orbiting the star outside of about 10 au, assuming the unseen planet would be embedded in the very broad planetesimal disk from a few to hundreds of astronomical units. We find that the distribution of dust detected interior to the broad outer belt is consistent with grains being dragged inward by the Poynting–Robertson effect. Under the drag-dominated disk assumption, tighter constraints can be derived for planets in specific locations; for example, any planet shepherding the inner edge of the outer belt is likely to be less than six Earth masses. The disk surface brightness profile along with the available infrared photometry suggest a disk inner edge near ~3-5 au, disconnected from the sub-astronomical-unit region that gives rise to the hot near-infrared excess. The gap between the hot, sub-astronomical-unit zone and the inner edge of the warm debris might be shepherded by a modest-mass, Neptune-size planet.

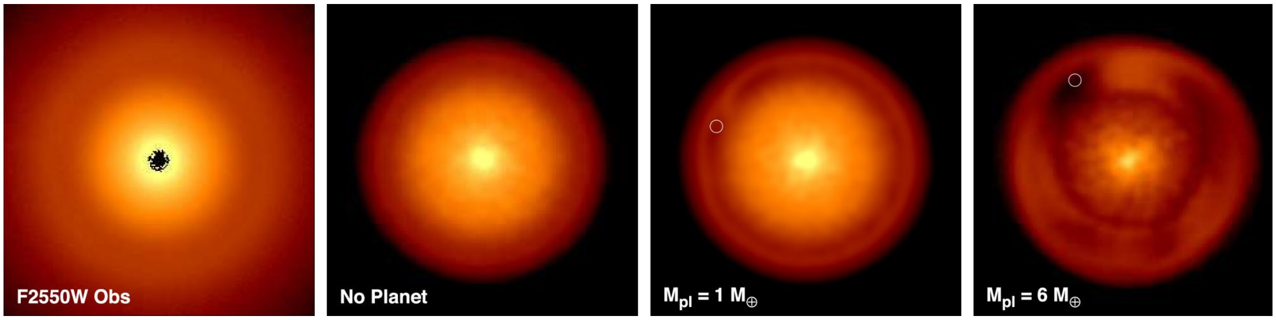

***Figure 8**. The model 25.5 µm disk morphology at 2 Myr for a PR-dominated disk, compared to the observed Vega F2550W image (first panel), all on the same display scale. The second panel assumes no planet (for details, see Section 5.2.2), while the third and fourth panels assume a 1 and 6 M $_\oplus$ mass planet at 65 au (marked by white circles), respectively (for details, see Section 5.2.3). The models do not include the entire outer planetesimal disk and halo, hence the difference with the observed images at large radii.*

Scalable, Advanced Machine Learning Based Approaches for Stellar Flare Identification: Application to TESS Short-cadence Data and Analysis of a New Flare Catalog

Lin, Chia-Lung; Apai, Dániel; Giampapa, Mark S.; Ip, Wing-Huen

➔ The Astronomical Journal, Volume 168, Issue 6, id.234, 31 pp.

We apply multialgorithm machine learning models to TESS 2 minute survey data from Sectors 1–72 to identify stellar flares. Models trained with deep neural network, random forest, and XGBoost algorithms utilize four flare light-curve characteristics as input features. Model performance is evaluated using the accuracy, precision, recall, and F 1 score metrics, all exceeding 94%. Validation against previously reported TESS M dwarf flare identifications shows that our models successfully recover over 92% of the flares while detecting ~2000 more small events, thus extending the detection sensitivity of previous work. After processing 1.3 million light curves, our models identify nearly 18,000 flare stars and 250,000 flares. We present an extensive catalog documenting both flare and stellar properties. We find strong correlations of total flare energy and flare amplitude with color, in agreement with previous studies. Flare frequency distributions are analyzed, refining power-law slopes for flare behavior with frequency uncertainties due to the detection incompleteness of low-amplitude events. We determine rotation periods for ~120,000 stars thus yielding the relationship between rotation period and flare activity. We find that the transition in rotation period between the saturated and unsaturated regimes in flare energy coincides with the same transition in rotation period separating the saturated and unsaturated levels in coronal X-ray emission. We find that X-ray emission increases more rapidly with flare luminosity in earlier-type and unsaturated stars, indicating more efficient coronal heating in these objects. Additionally, we detect flares in white dwarfs and hot subdwarfs, which likely arise from unresolved low-mass companions.

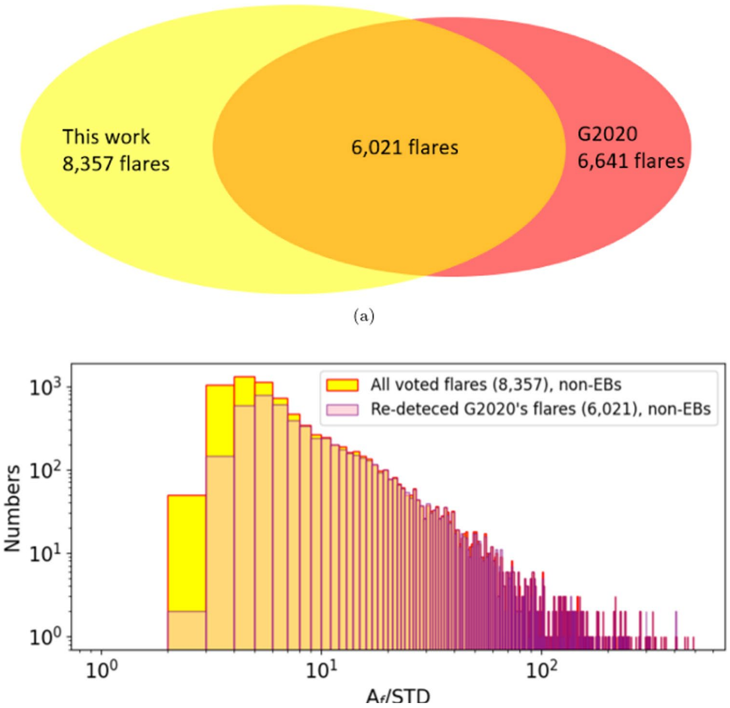

Figure 9. *(a) A Venn diagram illustrates the flares detected from the same TESS data set by M. N. Günther et al. (2020, red) and our models (yellow) and the detection overlap.*
(b)The Af/σ(FLC1) distributions of all voted flares (the flares recognized by at least two different machine learning models) and those also reported by M. N. Günther et al. (2020).

Large Interferometer For Exoplanets (LIFE): XIV. Finding terrestrial protoplanets in the galactic neighborhood

Cesario, Lorenzo; Lichtenberg, Tim; Alei, Eleonora; Carrión-González, Óscar; Dannert, Felix A.; Defrère, Denis; Ertel, Steve; Fortier, Andrea; García Muñoz, A.; Glauser, Adrian M.; Hansen, Jonah T.; Helled, Ravit; Huber, Philipp A.; Ireland, Michael J.; Kammerer, Jens; et al

➔ Astronomy & Astrophysics, Volume 692, id.A172, 18 pp.

Context. The increased brightness temperature of young rocky protoplanets during their magma ocean epoch makes them potentially amenable to atmospheric characterization at distances from the Solar System far greater than thermally equilibrated terrestrial exoplanets, offering observational opportunities for unique insights into the origin of secondary atmospheres and the near surface conditions of prebiotic environments. Aims. The Large Interferometer For Exoplanets (LIFE) mission will employ a space-based midinfrared nulling interferometer to directly measure the thermal emission of terrestrial exoplanets. In this work, we seek to assess the capabilities of various instrumental design choices of the LIFE mission concept for the detection of cooling protoplanets with transient high-temperature magma ocean atmospheres at the tail end of planetary accretion. In particular, we investigate the minimum integration times necessary to detect transient magma ocean exoplanets in young stellar associations in the Solar neighborhood. Methods. Using the LIFE mission instrument simulator (LIFEsim), we assessed how specific instrumental parameters and design choices, such as wavelength coverage, aperture diameter, and photon throughput, facilitate or disadvantage the detection of protoplan-ets. We focused on the observational sensitivities of distance to the observed planetary system, protoplanet brightness temperature (using a blackbody assumption), and orbital distance of the potential protoplanets around both G- and M-dwarf stars. Results. Our simulations suggest that LIFE will be able to detect (S/N ≥ 7) hot protoplanets in young stellar associations up to distances of 100 pc from the Solar System for reasonable integration times (up to a few hours). Detection of an Earth-sized protoplanet orbiting a Solar-sized host star at 1 AU requires less than 30 minutes of integration time. M-dwarfs generally need shorter integration times. The contribution from wavelength regions smaller than 6 µm is important for decreasing the detection threshold and discriminating emission temperatures. Conclusions. The LIFE mission is capable of detecting cooling terrestrial protoplanets within minutes to hours in several local young stellar associations hosting potential targets. The anticipated compositional range of magma ocean atmospheres motivates further architectural design studies to characterize the crucial transition from primary to secondary atmospheres.

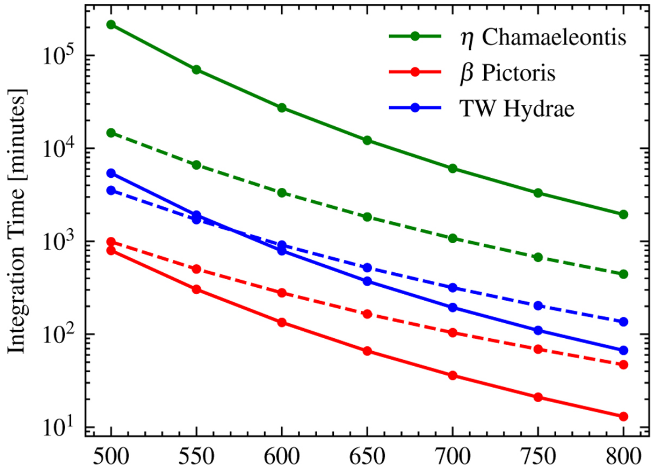

***Figure 2**. Moderate temperature cases: minimum integration times necessary for detection against the planet's emission temperature. The dashed lines represent the results for a Solar-sized star host at 1 AU, while the solid lines are for M-dwarfs at 0.13 AU. The associations are at distances of 37 pc (β Pictoris, red), 53 pc (TW Hydrae, blue), and 94 pc (η Chamaeleontis, green).*

A Search for Collisions and Planet–Disk Interactions in the Beta Pictoris Disk with 26 Years of High-precision HST/STIS Imaging

Avsar, Arin M.; Wagner, Kevin; Apai, Dániel; Stark, Christopher C. ; Wyatt, Mark C.

The Astrophysical Journal, Volume 975, Issue 1, id.40, 12 pp.

β Pictoris's well-studied debris disk and two known giant planets, in combination with the stability of the Hubble Space Telescope's Space Telescope Imaging Spectrograph (HST/STIS) (and now also JWST), offers a unique opportunity to test planet–disk interaction models and to observe recent planetesimal collisions. We present HST/STIS coronagraphic imaging from two new epochs of data taken between 2021 and 2023, complementing earlier data taken in 1997 and 2012. This data set enables a temporal comparison with the longest baseline and highest precision of any debris disk to date, with sensitivity to variations in temporal surface brightness of sub-percent levels in the midplane of the disk. While no localized changes in surface brightness are detected, which would be indicative of a recent planetesimal collision, there is a tentative brightening of the southeast side of the disk over the past decade. We link the constraints on surface brightness variations to dynamical models of the planetary system's evolution and to the collisional history of planetesimals. Using a coupled collisional model and injection/recovery framework, we estimate sensitivity to expanding collisional debris down to a Ceres mass per progenitor in the most sensitive regions of the disk midplane. These results demonstrate the capabilities of long-baseline, temporal studies with HST (and also soon with JWST) for constraining the physical processes occurring within debris disks.

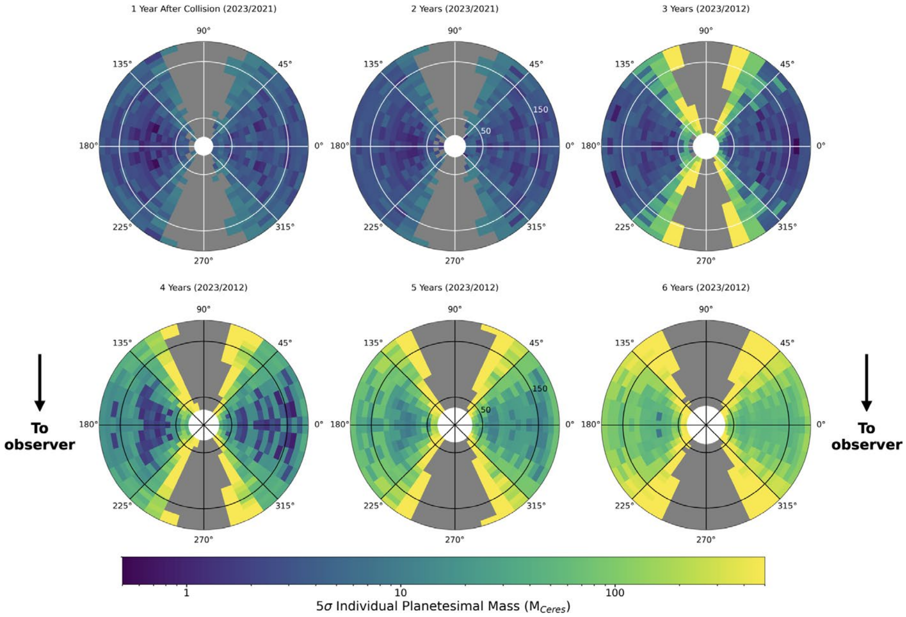

***Figure 6**. 5σ 2D collisional sensitivity maps for the β Pic disk. Each map shows the mass of a single collisional progenitor necessary to have a 5σ detection in our ratio maps. The epochs used in the ratio maps are given in parentheses in the title of each panel. The gray regions indicate regions in the disk blocked out by our coronagraphic wedge. The radial labels are shown in units of au. The maps are shown from a face-on perspective of the disk, and the black arrows indicate the direction to the observer. We can see a large increase in progenitor mass over the 6 years modeled, pointing to continual monitoring being essential to finding collisional remnants in scattered light observations and observing multi-wavelength evolution of the remnants.*

Geodynamics of Super-Earth GJ 486b

Meier, Tobias G.; Bower, Dan J.; Lichtenberg, Tim; Hammond, Mark; Tackley, Paul J.; Pierrehumbert, Raymond T.; Caballero, José A.; Tsai, Shang-Min; Weiner Mansfield, Megan; Tosi, Nicola; Baumeister, Philipp

Journal of Geophysical Research: Planets, Volume 129, Issue 10, article id. e2024JE008491

Many super-Earths are on very short orbits around their host star and, therefore, more likely to be tidally locked. Because this locking can lead to a strong contrast between the dayside and nightside surface temperatures, these super-Earths could exhibit mantle convection patterns and tectonics that could differ significantly from those observed in the present-day solar system. The presence of an atmosphere, however, would allow transport of heat from the dayside toward the nightside and thereby reduce the surface temperature contrast between the two hemispheres. On rocky planets, atmospheric and geodynamic regimes are closely linked, which directly connects the question of atmospheric thickness to the potential interior dynamics of the planet. Here, we study the interior dynamics of super-Earth GJ 486b (R=1.34 R⊕, M=3.0 M⊕, Teq≈700 K), which is one of the most suitable M-dwarf super-Earth candidates for retaining an atmosphere produced by degassing from the mantle and magma ocean. We investigate how the geodynamic regime of GJ 486b is influenced by different surface temperature contrasts by varying possible atmospheric circulation regimes. We also investigate how the strength of the lithosphere affects the convection pattern. We find that hemispheric tectonics, the surface expression of degree-1 convection with downwellings forming on one hemisphere and upwelling material rising on the opposite hemisphere, is a consequence of the strong lithosphere rather than surface temperature contrast. Anchored hemispheric tectonics, where downwellings und upwellings have a preferred (day/night) hemisphere, is favored for strong temperature contrasts between the dayside and nightside and higher surface temperatures.

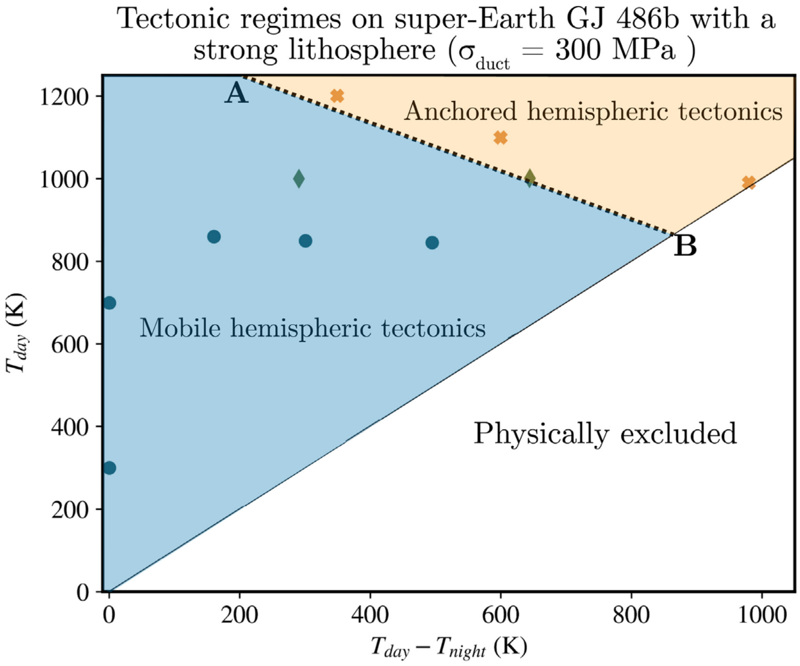

***Figure 13**. Overview of the tectonic regimes for the models with a strong lithosphere. An increased temperature contrast between the dayside and nightside as well as an increased (dayside) temperature increases the likelihood of anchored hemispheric tectonics (orange shaded region). For lower temperature contrasts and lower dayside temperatures, the mantle is in a mobile degree-1 convection regime with no preferred location for upwellings and downwellings (blue shaded region). The diamond markers indicate models from our study on LHS 3844b. The choice for the points (a) and (b) is explained in Section **4.2**. More model runs are necessary to determine where the transition from mobile to anchored hemispheric tectonics is. The white region is excluded as this would result in negative temperature on the nightside.*

An Analytic Characterization of the Limb Asymmetry—Transit Time Degeneracy

Murphy, Matthew M.; Beatty, Thomas G.; Apai, Dániel

➔ The Astrophysical Journal, Volume 974, Issue 2, id.179, 13 pp.

Atmospheres are not spatially homogeneous. This is particularly true for hot, tidally locked exoplanets with large day-to-night temperature variations, which can yield significant differences between the morning and evening terminators—known as limb asymmetry. Current transit observations with the James Webb Space Telescope (JWST) are precise enough to disentangle the separate contributions of these morning and evening limbs to the overall transmission spectrum in certain circumstances. However, the signature of limb asymmetry in a transit light curve is highly degenerate with uncertainty in the planet's time of conjunction. This raises the question of how precisely transit times must be measured to enable accurate studies of limb asymmetry, in particular with JWST. Although this degeneracy has been discussed in the literature, a general description of it has not been presented. In this work, we show how this degeneracy results from apparent changes in the transit contact times when the planetary disk has asymmetric limb sizes. We derive a general formula relating the magnitude of limb asymmetry to the amount by which it would cause the apparent time of conjunction to vary, which can reach tens of seconds. Comparing our formula to simulated observations, we find that numerical fitting techniques add additional bias to the measured time, of generally less than a second, resulting from the occultation geometry. We also derive an analytical formula for this extra numerical bias. These formulae can be applied to planning new observations or interpreting literature measurements, and we show examples for commonly studied exoplanets.

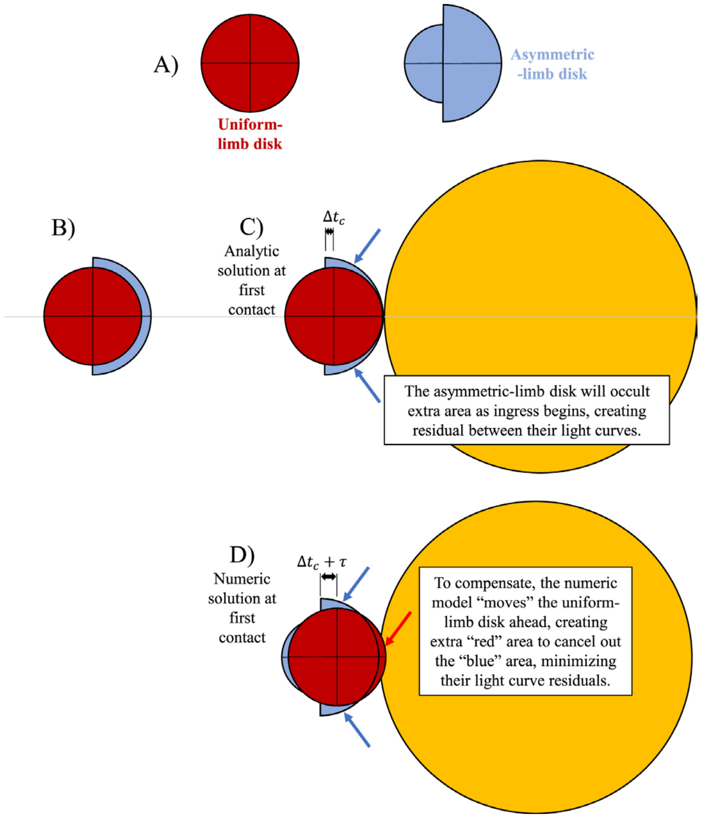

***Figure 5**. Schematic of the extra-area compensation problem. We generate a synthetic transit observation using the asymmetric-limb disk, shown in blue (Panel A). We fit these data using the uniform-limb disk shown in red. These two model planets are initially set to have the same time of conjunction t_c (Panel B). Due to limb asymmetry imprinted into the data, this fit will return a biased t_c when using this uniform-limb model. Panel (C) shows our analytic solution for this bias (Δt_c), which is the extra time the uniform-limb disk would travel until the two disks' first and last contact times are equal. This value of Δt_c is deemed a poor fit by the numeric model, however, as the "extra" occulting area of the asymmetric-limb disk in this arrangement leads to a large fitting residual. Rather, the numeric model prefers the solution shown in Panel (D) where the uniform-limb disk is translated even further ahead by time τ. In this arrangement, there is now "extra" occulting area for the uniform-limb disk, indicated by the red arrow, which cancels out the asymmetric-limb disk's extra area, leading to a minimized residual and thus a "better" fit.*

A Thermodynamic Criterion for the Formation of Circumplanetary Disks

Krapp, Leonardo; Kratter, Kaitlin M.; Youdin, Andrew N.; Benítez-Llambay, Pablo; Masset, Frédéric; Armitage, Philip J.

➔ The Astrophysical Journal, Volume 973, Issue 2, id.153, 15 pp.

The formation of circumplanetary disks is central to our understanding of giant planet formation, influencing their growth rate during the post-runaway phase and observability while embedded in protoplanetary disks. We use three-dimensional global multifluid radiation hydrodynamics simulations with the FARGO3D code to define the thermodynamic conditions that enable circumplanetary disk formation around Jovian planets on wide orbits. Our simulations include stellar irradiation, viscous heating, static mesh refinement, and active calculation of opacity based on multifluid dust dynamics. We find a necessary condition for the formation of circumplanetary disks in terms of a mean cooling time: When the cooling time is at least 1 order of magnitude shorter than the orbital timescale, the specific angular momentum of the gas is nearly Keplerian at scales of one-third of the Hill radius. We show that the inclusion of multifluid dust dynamics favors rotational support because dust settling produces an anisotropic opacity distribution that favors rapid cooling. In all our models with radiation hydrodynamics, specific angular momentum decreases as time evolves, in agreement with the formation of an inner isentropic envelope due to compressional heating. The isentropic envelope can extend up to one-third of the Hill radius and shows negligible rotational support. Thus, our results imply that young gas giant planets may host spherical isentropic envelopes, rather than circumplanetary disks.

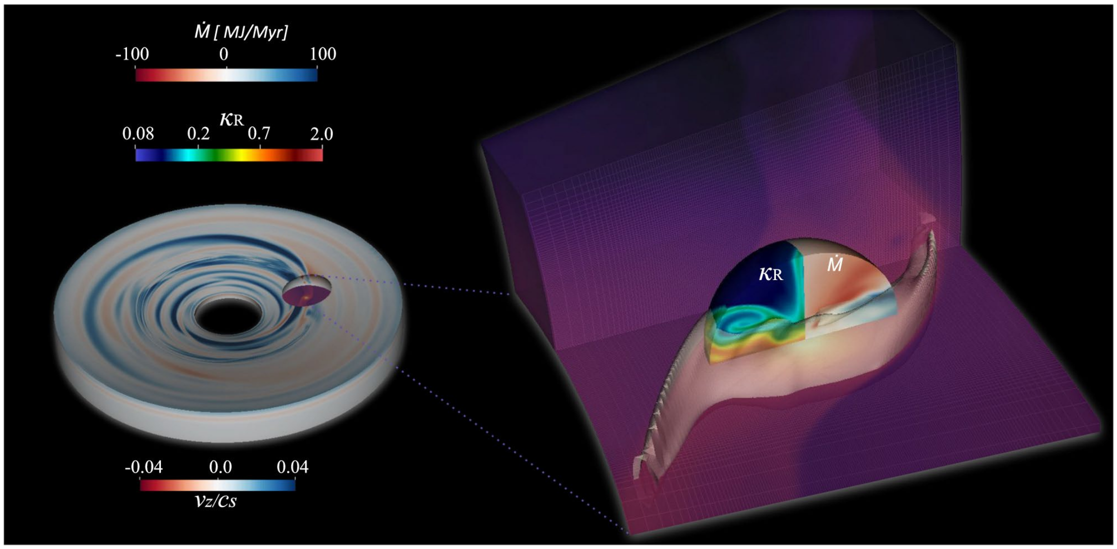

***Figure 1**. Global multifluid model after two orbits. The local patch shows the opacity and mass flux (in units of Jupiter mass per year) at the scales of the Hill sphere. The background magenta color displays the gas density for reference. The inclusion of dust dynamics introduces an anisotropic opacity distribution in the radiative transfer model, which agrees with the opacity distribution estimated with isothermal models in Krapp et al. (2022). The mass flux balances between polar inflow (red color) and midplane outflow (blue color). The surface contour corresponds to an isodensity with* $\rho_g = 3.5 \times 10^{-12}$ *g cm*$^{-3}$ *that maps the initial envelope. This envelope will become more spherically symmetric as time evolves and rotational support is weakened. The global disk on the left shows the vertical velocity of the gas. The static mesh refinement allows us to solve the dynamics inside the Hill sphere as well as the large-scale flow exited by the planet.*

TESS discovery of two super-Earths orbiting the M-dwarf stars TOI-6002 and TOI-5713 near the radius valley

Ghachoui, M. ; Rackham, B. V.; Dévora-Pajares, M. ; Chouqar, J. ; Timmermans, M. ; Kaltenegger, L. ; Sebastian, D. ; Pozuelos, F. J.; Eastman, J. D. ; Burgasser, A. J. ; Murgas, F.; Stassun, K. G. ; Gillon, M. ; Benkhaldoun, Z.; Palle, E. ; Delrez, L. ; Jenkins, J. M. ; Barkaoui, K. ; Narita, N. ; de Leon, J. P. ; Mori, M. ; Shporer, A. ; Rowden, P. ; Kostov, V. ; Fűrész, G. ; Collins, K. A. ; Schwarz, R. P. ; Charbonneau, D. ; Guerrero, N. M. ; Ricker, G. ; Jehin, E. ; Fukui, A. ; Kawai, Y. ; Hayashi, Y. ; Esparza-Borges, E. ; Parviainen, H. ; Clark, C. A.; Ciardi, D. R. ; Polanski, A. S. ; Schleider, J. ; Gilbert, E. A. ; Crossfield, I. J. M. ; Barclay, T. ; Dressing, C. D. ; Karpoor, P. R. ; Softich, E. ; Gerasimov, R. ; Davoudi, F.

➔ Astronomy & Astrophysics, Volume 690, id.A263, 19 pp.

We present the validation of two TESS super-Earth candidates transiting the mid-M dwarfs TOI-6002 and TOI-5713 every 10.90 and 10.44 days, respectively. The first star (TOI-6002) is located 32.038 ± 0.019 pc away, with a radius of 0.2409-0.0065+0.0066 R⊙, a mass of 0.2105-0.0048+0.0049 M⊙, and an effective temperature of 3229-57+77 K. The second star (TOI-5713) is located 40.946 ± 0.032 pc away, with a radius of 0.2985-0.0072+0.0073 R⊙, a mass of 0.2653 ± 0.0061 M⊙, and an effective temperature of 3225-40+41 K. We validated the planets using TESS data, ground-based multi-wavelength photometry from many ground-based facilities, as well as high-resolution AO observations from Keck/NIRC2. TOI-6002 b has a radius of 1.65-0.19+0.22 R⊕ and receives 1.77-0.110.16S⊕. TOI-5713 b has a radius of 1.77-0.11+0.13 R⊕ and receives 2.42 ± 0.11S⊕. Both planets are located near the radius valley and near the inner edge of the habitable zone of their host stars, which makes them intriguing targets for future studies to understand the formation and evolution of small planets around M-dwarf stars.

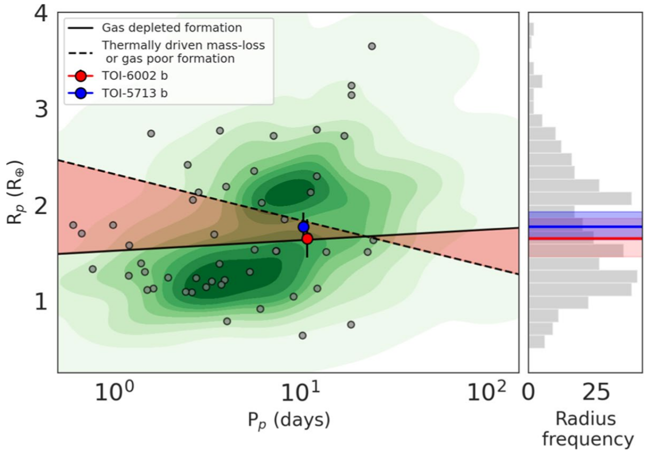

Figure 10. *Distribution of planet radii and orbital periods for all confirmed small planets hosted by low-mass stars ($M_* \lesssim 0.65\ M_\odot$). The solid line represents the predicted location of the radius valley based on the gas-depleted formation model (Cloutier & Menou 2020). The dashed line shows the predicted location of the valley for the thermally-driven photoevaporation and gas-poor formation models (Van Eylen et al. 2018). The red and blue dots represents the planets TOI-6002b and TOI-5713b, respectively. The 1D radius distribution, with the location of the two planets, is shown on the right panel.*

Mass determination of two Jupiter-sized planets orbiting slightly evolved stars: TOI-2420 b and TOI-2485 b

Carleo, Ilaria ; Barrágan, Oscar ; Persson, Carina M. ; Fridlund, Malcolm ; Lam, Kristine W. F. ; Messina, Sergio ; Gandolfi, Davide ; Smith, Alexis M. S. ; Johnson, Marshall C. ; Cochran, William ; Osborne, Hannah L. M. ; Brahm, Rafael ; Ciardi, David R. ; Collins, Karen A. ; Everett, Mark E. ; Giacalone, Steven ; Guenther, Eike W. ; Hatzes, Artie ; Hellier, Coel ; Horner, Jonathan ; Kabáth, Petr ; Korth, Judith ; MacQueen, Phillip ; Masseron, Thomas ; Murgas, Felipe; Nowak, Grzegorz ; Rodriguez, Joseph E. ; Watkins, Cristilyn N. ; Wittenmyer, Rob ; Zhou, George ; Ziegler, Carl ; Bieryla, Allyson ; Boyd, Patricia T. ; Clark, Catherine A.; Dressing, Courtney D. ; Eastman, Jason D. ; Eberhardt, Jan ; Endl, Michael ; Espinoza, Nestor ; Fausnaugh, Michael ; Guerrero, Natalia M. ; Henning, Thomas ; Hesse, Katharine ; Hobson, Melissa J. ; Howell, Steve B. ; Jordán, Andrés ; Latham, David W. ; Lund, Michael B. ; Mireles, Ismael ; Narita, Norio ; Tala Pinto, Marcelo; Pugh, Teznie ; Quinn, Samuel N. ; Ricker, George ; Rodriguez, David R. ; Rojas, Felipe I. ; Rose, Mark E. ; Rudat, Alexander ; Sarkis, Paula ; Savel, Arjun B. ; Schlecker, Martin ; Schwarz, Richard P. ; Seager, Sara ; Shporer, Avi ; Smith, Jeffrey C. ; Stassun, Keivan G. ; Stockdale, Chris ; Trifonov, Trifon ; Vanderspek, Roland ; Winn, Joshua N. ; Wright, Duncan

Astronomy & Astrophysics, Volume 690, id.A18, 14 pp.

Context. Hot and warm Jupiters might have undergone the same formation and evolution path, but the two populations exhibit different distributions of orbital parameters. This challenges our understanding of their actual origin. Aims. We report the results of our warm Jupiters survey, which was carried out with the CHIRON spectrograph within the KESPRINT collaboration. We addressed the question of the population origin by studying two planets that might help to bridge the gap between the two populations. Methods. We confirm two planets and determine their mass. One is a hot Jupiter (with an orbital period shorter than 10 days), TOI-2420 b, and the other is a warm Jupiter, TOI-2485 b. We analyzed them using a wide variety of spectral and photometric data in order to characterize these planetary systems. Results. We found that TOI-2420 b has an orbital period of Pb=5.8 days, a mass of Mb=0.9 MJ, and a radius of Rb=1.3 RJ, with a planetary density of 0.477 g cm-3. TOI-2485 b has an orbital period of Pb=11.2 days, a mass of Mb=2.4 MJ, and a radius of Rb=1.1 RJ with a density of 2.36 g cm-3. Conclusions. With the current parameters, the migration history for TOI-2420 b and TOI-2485 b is unclear: Scenarios of a high-eccentricity migration cannot be ruled out, and the characteristics of TOI-2485 b even support this scenario.

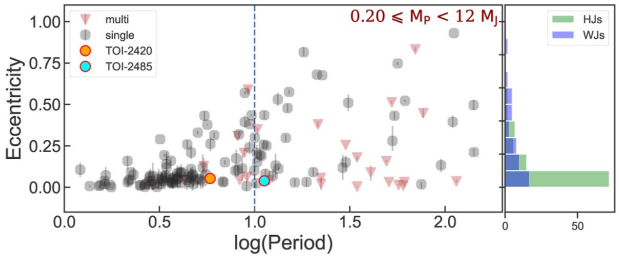

Figure 9. *Eccentricity distribution as a function of the orbital period for Jupiter-sized planets (data taken as of UT 2024 March 13). The dashed blue line represents the 10-day boundary between HJs and WJs. The orange point represents TOI-2420 b, and the cyan point represents TOI-2485 b. The red triangles represent the planets in multiplanet systems.*

The First Evidence of a Host Star Metallicity Cutoff in the Formation of Super-Earth Planets

Boley, Kiersten M.; Christiansen, Jessie L.; Zink, Jon; Hardegree-Ullman, Kevin; Lee, Eve J.; Hopkins, Philip F.; Wang, Ji; Fernandes, Rachel B.; Bergsten, Galen J.; Bhure, Sakhee

➔ The Astronomical Journal, Volume 168, Issue 3, id.128, 8 pp.

Planet formation is expected to be severely limited in disks of low metallicity, owing to both the small solid mass reservoir and the low-opacity accelerating the disk gas dissipation. While previous studies have found a weak correlation between the occurrence rates of small planets ($\lesssim 4R_{\oplus}$) and stellar metallicity, so far no studies have probed below the metallicity limit beyond which planet formation is predicted to be suppressed. Here, we constructed a large catalog of ~110,000 metal-poor stars observed by the TESS mission with spectroscopically derived metallicities, and systematically probed planet formation within the metal-poor regime ([Fe/H] $\leq$-0.5) for the first time. Extrapolating known higher-metallicity trends for small, short-period planets predicts the discovery of ~68 super-Earths around these stars (~85,000 stars) after accounting for survey completeness; however, we detect none. As a result, we have placed the most stringent upper limit on super-Earth occurrence rates around metal-poor stars (-0.75 < [Fe/H] $\leq$ -0.5) to date, $\leq$ 1.67%, a statistically significant (p-value = 0.000685) deviation from the prediction of metallicity trends derived with Kepler and K2. We find a clear host star metallicity cliff for super-Earths that could indicate the threshold below which planets are unable to grow beyond an Earth-mass at short orbital periods. This finding provides a crucial input to planet-formation theories, and has implications for the small planet inventory of the Galaxy and the galactic epoch at which the formation of small planets started.

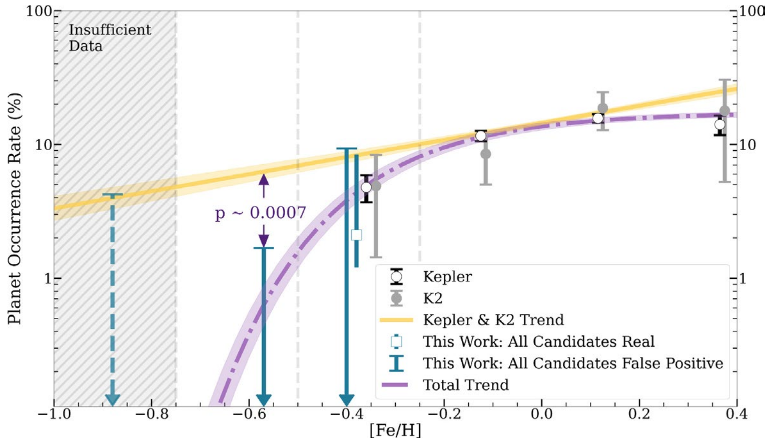

***Figure 5**. Super-Earth occurrence for Kepler (black circles) and K2 (gray circles), TESS data assuming all candidates are real (teal square), and 99.7% confidence intervals to calculate the upper limits for TESS data assuming all candidates are false positives (teal triangles) as a function of metallicity. The [−0.25, −0.5] bin occurrence rates are offset horizontally for visual clarity. The best-fit power-law trend line for the Kepler and K2 data (yellow) is displayed and extrapolated to [Fe/H] = −0.75 showing the 1σ uncertainties (Zink et al. 2023). We show the combined best-fit exponential trend line for Kepler, K2, and TESS (purple; Equation (6)) including the 1σ uncertainties. Each metallicity bin is indicated by gray dashed lines. Within the [−0.75, −1] bin, there is insufficient data to further constrain the super-Earth occurrence rate as a function of metallicity (denoted by the gray hatched region).*

Assessing Exoplanetary System Architectures with DYNAMITE Including Observational Upper Limits

Dietrich, Jamie

The Astronomical Journal, Volume 168, Issue 3, id.119, 13 pp.

The information gathered from observing planetary systems is not limited to the discovery of planets, but also includes the observational upper limits constraining the presence of any additional planets. Incorporating these upper limits into statistical analyses of individual systems can significantly improve our ability to find hidden planets in these systems by narrowing the parameter space in which to search. Here, I include radial velocity (RV), transit, and transit timing variation (TTV) upper limits on additional planets in known multiplanet systems into the DYNAMITE software package and test their impact on the predicted planets for these systems. The tests are run on systems with previous DYNAMITE analysis and with updated known planet parameters in the 2–3 yr since the original predictions. I find that the RV limits provide the strongest constraints on additional planets, lowering the likelihood of finding them within orbital periods of $\sim$ 10–100 days in the inner planetary systems, as well as truncating the likely planet size (radius and/or mass) distributions toward planets smaller than those currently observed. Transit and TTV limits also provide information on the size and inclination distributions of both the known and predicted planets in the system. Utilizing these limits on a wider range of systems in the near future will help determine which systems might be able to host temperate terrestrial planets and contribute to the search for extraterrestrial biosignatures.

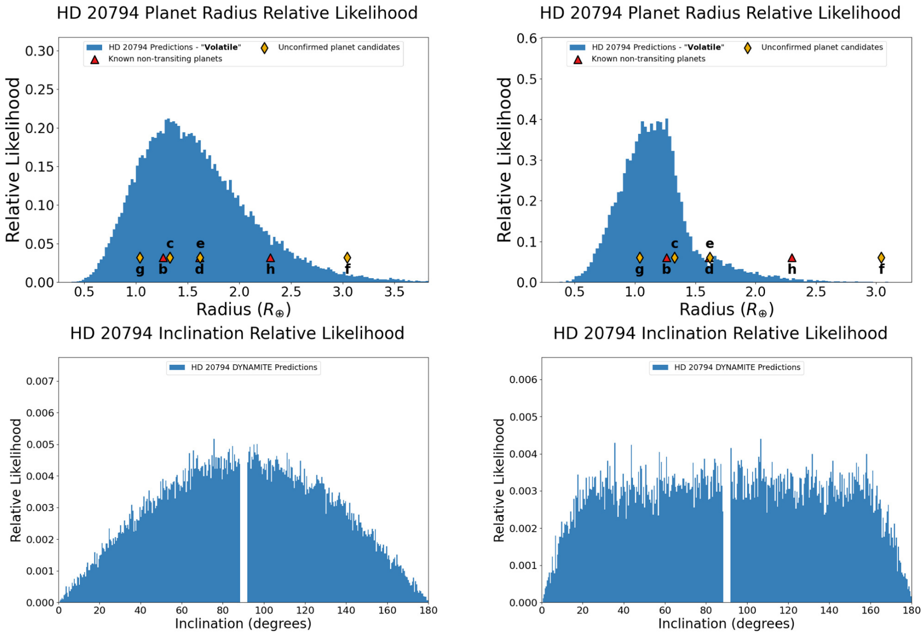

Figure 9*. DYNAMITE predictions for the planet radius (top) and orbital inclination (bottom) for no RV limits (left) and 25 cm s^{-1} RV limits (right). The planet radius distribution is calculated using the Otegi et al. (2020) M–R relationship and a draw from the inclination distribution to get the hypothetical mass from the msini value. The strict RV limit significantly lowers the likelihood of higher-mass planets as well as planets closer to an edge-on orbital inclination, as both of these would have higher RV semi-amplitudes.*

Rocky planet formation in compact disks around M dwarfs

Sanchez, M.; van der Marel, N. ; Lambrechts, M. ; Mulders, G. D. ; Guerra-Alvarado, O. M.

Astronomy & Astrophysics, Volume 689, id.A236, 25 pp.

Context. Due to the improvements in radial velocity and transit techniques, we know that rocky or rocky-icy planets, in particular close-in super-Earths in compact configurations, are the most common ones around M dwarfs. On the other hand, thanks to the high angular resolution of ALMA we know that many disks around very low-mass stars (between 0.1 and 0.5 $M_\odot$) are rather compact and small (without observable substructures and radius less than 20 au), which favors the idea of an efficient radial drift that could enhance planet formation in the terrestrial zone. Aims. Our aim was to investigate the potential formation paths of the observed close-in rocky exoplanet population around M dwarfs, especially close-in super-Earths, assuming that planet formation could take place in compact disks with an efficient dust radial drift. Methods. We developed N-body simulations that include a sample of embryos growing by pebble accretion exposed to planet-disk interactions, star-planet tidal interactions, and general relativistic corrections that include the evolution of the luminosity, radius, and rotational period of the star. For a star of 0.1 $M_\odot$, we considered different gas disk viscosities and initial embryo distributions. We also explored planet formation by pebble accretion around stars of 0.3 $M_\odot$ and 0.5 $M_\odot$. Lastly, for each stellar mass, we ran simulations that include a sample of embryos growing by planetesimal accretion instead of pebble accretion. Results. Our main result is that the sample of simulated planets that grow by pebble accretion in a gas disk with low viscosity (α = 10-4) can reproduce the close-in low-mass exoplanet population around M dwarfs in terms of multiplicity, mass, and semi-major axis. Furthermore, we found that a gas disk with high viscosity (α = 10-3), and thus lower pebble accretion rates, cannot reproduce the observed planet masses as no planet more massive than 0.5 $M_\oplus$ could be formed in our simulations. In addition, we show that planetesimal accretion favors the formation of smaller planets than pebble accretion does. Whether this planet population truly exists remains unknown with the current instrumental sensitivity. Conclusions. Rocky planet formation around M dwarfs can take place in compact and small dust disks driven by an efficient radial drift in a gas disk with low viscosity (α = 10-4). This result points toward a new approach in the direction of the disk conditions needed for rocky planet formation around very low-mass stars.

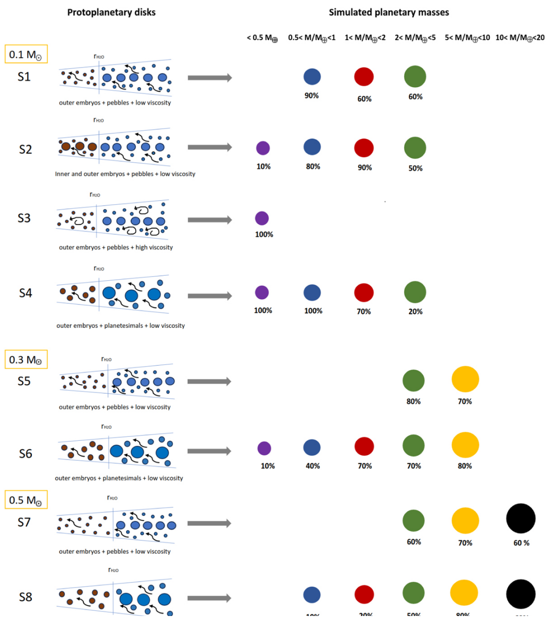

***Figure 4**. Graphic overview of the disks and final simulated planets in each formation scenario. Left: embryos of different masses (the biggest circles), and pebbles (the smallest circles) or planetesimals (medium circles) located either inside (brown) or outside (blue) the H_2O snowline in a gas disk with low viscosity (curved black arrows) or high viscosity (spiral black arrows). Right: planets with masses <0.5 $M_\odot$ (violet circles), 0.5 < $M/M_\oplus$ < 1 (blue circles), 1 < $M/M_\oplus$ < 2 (red circles), 2 < $M/M_\oplus$ < 5 (green circles), 5 < $M/M_\oplus$ < 10 (yellow circles) and 10 < $M/M_\oplus$ < 20 (black circles). The percentage of simulations in which planets in each mass range were formed is given below the circles.*

Revisiting the dynamical masses of the transiting planets in the young AU Mic system: Potential AU Mic b inflation at 20 Myr

Mallorquín, M. ; Béjar, V. J. S. ; Lodieu, N. ; Zapatero Osorio, M. R. ; Yu, H. ; Suárez Mascareño, A.; Damasso, M. ; Sanz-Forcada, J. ; Ribas, I. ; Reiners, A. ; Quirrenbach, A. ; Amado, P. J. ; Caballero, J. A.; Aigrain, S. ; Barragán, O. ; Dreizler, S. ; Fernández-Martín, A.; Goffo, E. ; Henning, Th. ; Kaminski, A. ; Klein, B. ; Luque, R. ; Montes, D.; Morales, J. C. ; Nagel, E. ; Pallé, E. ; Reffert, S. ; Schlecker, M. ; Schweitzer, A.

➔ Astronomy & Astrophysics, Volume 689, id.A132, 28 pp.

Context. Understanding planet formation is important in the context of the origin of planetary systems in general and of the Solar System in particular, as well as to predict the likelihood of finding Jupiter, Neptune, and Earth analogues around other stars. Aims. We aim to precisely determine the radii and dynamical masses of transiting planets orbiting the young M star AU Mic using public photometric and spectroscopic datasets. Methods. We performed a joint fit analysis of the TESS and CHEOPS light curves and more than 400 high-resolution spectra collected with several telescopes and instruments. We characterise the stellar activity and physical properties (radius, mass, density) of the transiting planets in the young AU Mic system through joint transit and radial velocity fits with Gaussian processes. Results. We determine a radius of Rpb = 4.79 ± 0.29 R⊕, a mass of Mpb = 9.0 ± 2.7 M⊕, and a bulk density of ρpb = 0.49 ± 0.16 g cm-3 for the innermost transiting planet AU Mic b. For the second known transiting planet, AU Mic c, we infer a radius of Rpc = 2.79 ± 0.18 R⊕, a mass of Mpc = 14.5 ± 3.4 M⊕, and a bulk density of ρpc = 3.90 ± 1.17 g cm-3. According to theoretical models, AU Mic b may harbour an H2 envelope larger than 5% by mass, with a fraction of rock and a fraction of water. AU Mic c could be made of rock and/or water and may have an H2 atmosphere comprising at most 5% of its mass. AU Mic b has retained most of its atmosphere but might lose it over tens of millions of years due to the strong stellar radiation, while AU Mic c likely suffers much less photo-evaporation because it lies at a larger separation from its host. Using all the datasets in hand, we determine a 3 σ upper mass limit of Mp[d] sin i = 8.6 M⊕ for the AU Mic'd' TTV-candidate. In addition, we do not confirm the recently proposed existence of the planet candidate AU Mic 'e' with an orbital period of 33.4 days. We investigated the level of the radial velocity variations and show that it is lower at longer wavelength with smaller changes from one observational campaign to another.

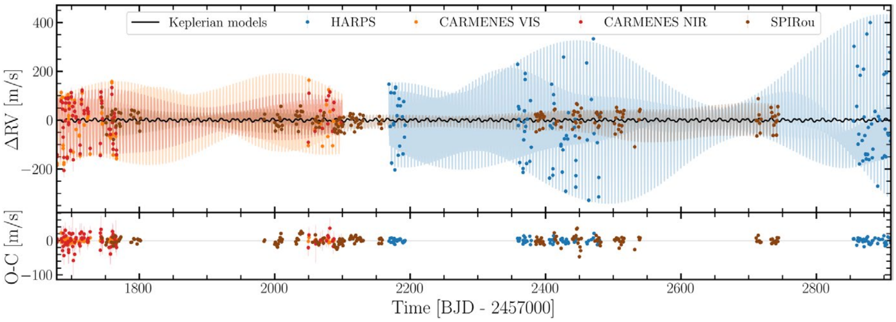

***Figure 10**. CARMENES VIS, CARMENES NIR, HARPS, and SPIRou RV data for AU Mic. Top panel: individual activity models (coloured lines) and combined Keplerian models for the planets (black line). Bottom panel: residuals for the best-fit.*

Challenge of direct imaging of exoplanets within structures: disentangling real signal from point source from background light

Li, Jialin; Close, Laird M.; Males, Jared R.; Haffert, Sebastiaan Y.; Weinberger, Alycia; Follette, Katherine; Wagner, Kevin; Apai, Daniel; Wu, Ya-Lin; Long, Joseph D.; Perez, Laura; Pearce, Logan A.; Kueny, Jay K.; McEwen, Eden A.; Van Gorkom, Kyle; Guyon, Olivier; Kautz, Maggie Y.; Hedglen, Alexander D.; Foster, Warren B.; Roberts, Roz; Lumbres, Jennifer; Schatz, Lauren

➔ Proceedings of the SPIE, Volume 13097, id. 1309714 14 pp. (2024)

The high contrast and spatial resolution requirements for directly imaging exoplanets requires effective coordination of wavefront control, coronagraphy, observation techniques, and post-processing algorithms. However, even with this suite of tools, identifying and retrieving exoplanet signals embedded in resolved scattered light regions can be extremely challenging due to the increased noise from scattered light off the circumstellar disk and the potential misinterpretation of the true nature of the detected signal. This issue pertains not only to imaging terrestrial planets in habitable zones within zodiacal and exozodiacal emission but also to young planets embedded in circumstellar, transitional, and debris disks. This is particularly true for Hα detection of exoplanets in transitional disks. This work delves into recent Hα observations of three transitional disks systems with MagAO-X, an extreme adaptive optics system for the 6.5-meter Magellan Clay telescope. We employed angular differential imaging (ADI) and simultaneous spectral differential imaging (SSDI) in combination with KLIP, a PCA algorithm in post-processing, for optimal starlight suppression and quasi-static noise removal. We discuss the challenges in protoplanet identification with MagAO-X in environments rich with scattered and reflected light from disk structures and explore a potential solution for removing noise contributions from real astronomical objects with current observation and post-processing techniques.

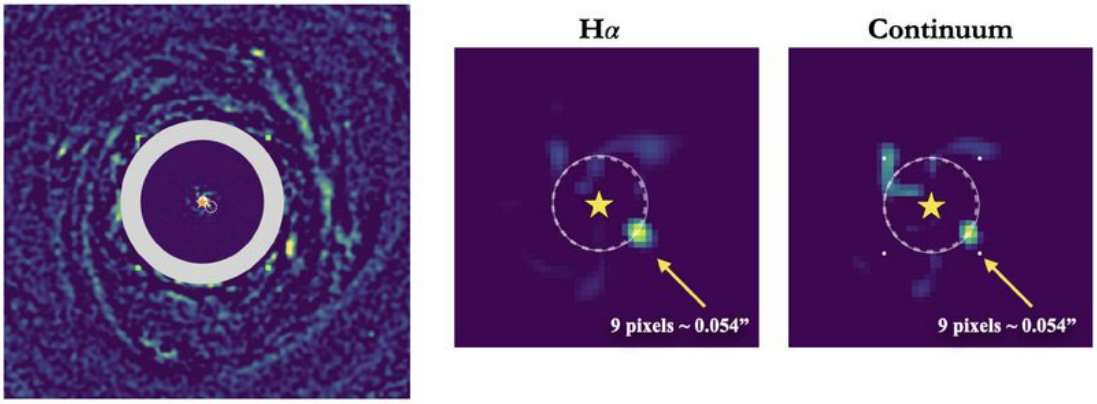

***Figure 1**. The composite reduced KLIP (movement=1, numbasis=5, High Pass (HP) filter width=4.5 pixels) in Hα continuum showcasing the multi-spiral Disk with the full frame FOV of ~2.5” by 2.5”. Note north is up and east is left. The grey annulus indicates the change in stretch in this image. The stellar companion, HD 142527B, can be seen more clearly in the Hα and continuum images respectively in the middle and right panels. The circle aperture marks a 3 pixel radius around the location of the stellar binary. The excess Hα flux from HD 142527B is clear and the continuum flux is likely emission from the photosphere of this low mass M star.*

TOI-2447 b / NGTS-29 b: a 69-day Saturn around a Solar analogue

Gill, Samuel ; Bayliss, Daniel; Ulmer-Moll, Solène ; Wheatley, Peter J.; Brahm, Rafael ; Anderson, David R.; Armstrong, David; Apergis, Ioannis; Alves, Douglas R.; Burleigh, Matthew R.; Butler, R. P. ; Bouchy, François ; Battley, Matthew P. ; Bryant, Edward M.; Bieryla, Allyson; et al

Monthly Notices of the Royal Astronomical Society, Volume 532, Issue 2, pp.1444-1458

Discovering transiting exoplanets with relatively long orbital periods (>10 d) is crucial to facilitate the study of cool exoplanet atmospheres (Teq < 700 K) and to understand exoplanet formation and inward migration further out than typical transiting exoplanets. In order to discover these longer period transiting exoplanets, long-term photometric, and radial velocity campaigns are required. We report the discovery of TOI-2447 b (=NGTS-29 b), a Saturn-mass transiting exoplanet orbiting a bright (T = 10.0) Solar-type star (Teff = 5730 K). TOI-2447 b was identified as a transiting exoplanet candidate from a single transit event of 1.3 per cent depth and 7.29 h duration in TESS Sector 31 and a prior transit event from 2017 in NGTS data. Four further transit events were observed with NGTS photometry which revealed an orbital period of P = 69.34 d. The transit events establish a radius for TOI-2447 b of 0.865±0.010RJ, while radial velocity measurements give a mass of 0.386±0.025MJ. The equilibrium temperature of the planet is 414 K, making it much cooler than the majority of TESS planet discoveries. We also detect a transit signal in NGTS data not caused by TOI-2447 b, along with transit timing variations and evidence for a ~150 d signal in radial velocity measurements. It is likely that the system hosts additional planets, but further photometry and radial velocity campaigns will be needed to determine their parameters with confidence. TOI-2447 b/NGTS-29 b joins a small but growing population of cool giants that will provide crucial insights into giant planet composition and formation mechanisms.

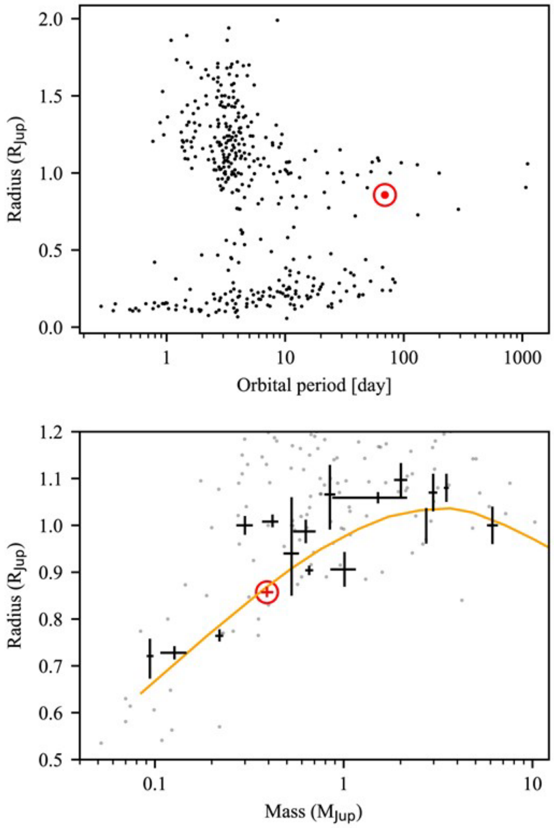

***Figure 10**. Upper panel: Radius-period diagram of well-characterized transiting exoplanets (mass to better than 50 per cent precision and radius to better than 20 per cent; exoplanetarchive.ipac.caltech.edu, accessed 2022-10-07). TOI-2447 b/NGTS-29 b is indicated in red. Lower panel: Mass–radius diagram for giant exoplanets from the same sample. Planets with orbital periods longer than 30 d are plotted in black, those with periods shorter than 30 d in grey. TOI-2447 b is indicated in red with an outer circle. The orange line shows a theoretical mass–radius relation for a cold hydrogen/helium exoplanet (Seager et al. 2007).*

Repelling Planet Pairs by Ping-pong Scattering

Wu, Yanqin; Malhotra, Renu; Lithwick, Yoram

The Astrophysical Journal, Volume 971, Issue 1, id.5, 11 pp.

The Kepler mission reveals a peculiar trough-peak feature in the orbital spacing of close-in planets near mean-motion resonances: a deficit and an excess that are, respectively, a couple of percent interior to and wide of the resonances. This feature has received two main classes of explanations: one involving eccentricity damping and the other scattering with small bodies. Here, we point out a few issues with the damping scenario and study the scattering scenario in more detail. We elucidate why scattering small bodies tends to repel two planets. As the small bodies random-walk in energy and angular momentum space, they tend to absorb fractionally more energy than angular momentum. This, which we call "ping-pong repulsion," transports angular momentum from the inner to the outer planet and pushes the two planets apart. Such a process, even if ubiquitous, leaves identifiable marks only near first-order resonances: diverging pairs jump across the resonance quickly and produce the mean-motion resonance asymmetry. To explain the observed positions of the trough-peaks, a total scattering mass of order a few percent of the planet masses is required. Moreover, if this mass is dominated by a handful of Mercury-sized bodies, one can also explain the planet eccentricities as inferred from transit-time variations. Last, we suggest how these conditions may have naturally arisen during the late stages of planet formation.

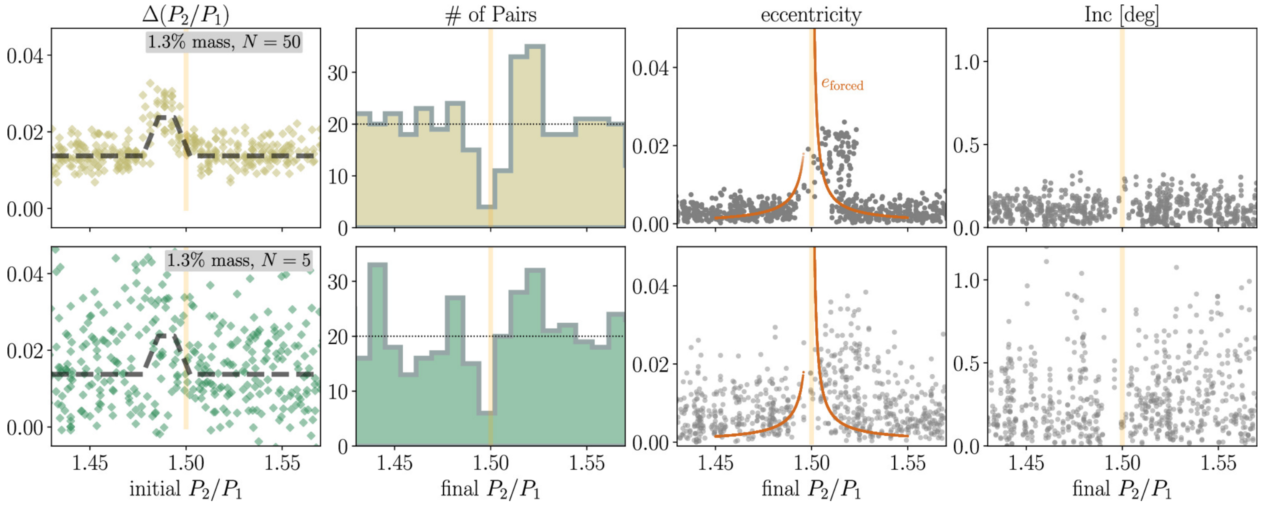

Figure 9*. Comparing detailed simulation results using light (top) and heavy (bottom) ping-pongs, for the same total mass of ϵ = 1.3%. Each ping-pong in the top panel has a mass equal to 0.08 that of Mercury, while those in the bottom have masses equal to 0.8 that of Mercury. The left-most panels show the amount of repulsion, with the thick dashed lines indicating the so-called “continuum limit” (Equations (5)–(6)). The left middle panels show the initial (dotted lines) and final (colored histogram) distributions in P_2/P_1. The bottom group exhibits a larger Poisson noise, translating into a more jagged period distribution and a less well-defined resonance asymmetry. The panels to the right show the final planet eccentricities and inclinations. Planets in the upper group are only weakly excited, with eccentricity kicks from resonance crossing clearly visible. In contrast, the bottom group are excited to values that, if described by Rayleigh distributions, have modes of $\sigma_e \sim 0.008$ and $\sigma_{inc} \sim \sigma_e/2 \sim 0.004$ radian (or 0.25 deg).*

Toward Robust Corrections for Stellar Contamination in JWST Exoplanet Transmission Spectra

Rackham, Benjamin V.; de Wit, Julien

➔ The Astronomical Journal, Volume 168, Issue 2, id.82, 16 pp.

Transmission spectroscopy is still the preferred characterization technique for exoplanet atmospheres, although it presents unique challenges that translate into characterization bottlenecks when robust mitigation strategies are missing. Stellar contamination is one such challenge that can overpower the planetary signal by up to an order of magnitude, and thus not accounting for it can lead to significant biases in the derived atmospheric properties. Yet this accounting may not be straightforward, as important discrepancies exist between state-of-the-art stellar models and measured spectra and between models themselves. Here we explore the extent to which stellar models can be used to reliably correct for stellar contamination and yield a planet's uncontaminated transmission spectrum. We find that discrepancies between stellar models can significantly contribute to the noise budget of JWST transmission spectra of planets around stars with heterogeneous photospheres, the true number of unique photospheric spectral components and their properties can only be accurately retrieved when the stellar models have sufficient fidelity, and under such optimistic circumstances the contribution of stellar contamination to the noise budget of a transmission spectrum is considerably below that of the photon noise for the standard transit observation setup. Therefore, we advocate for further development of model spectra of stars and their active regions in a data-driven manner, empirical approaches for deriving spectra of photospheric components using the observatories with which the atmospheric explorations are carried out, and analysis techniques accounting for multimodal posterior distributions for photospheric parameters of interest, which will be increasingly revealed by precise JWST measurements.

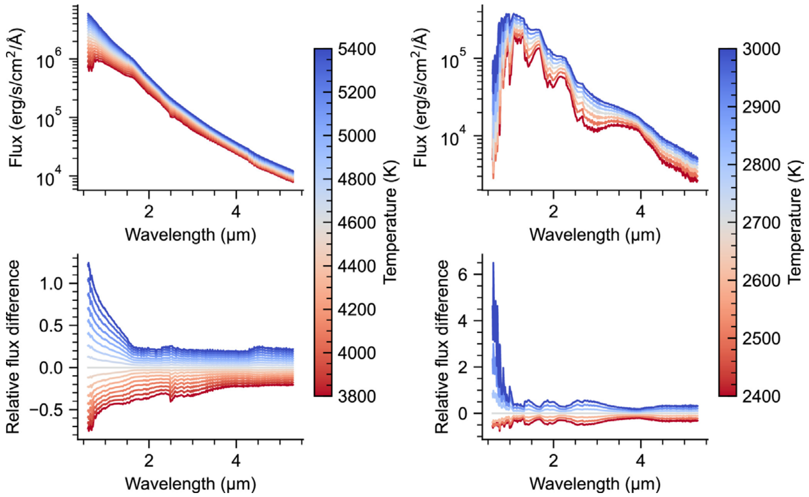

***Figure 7**. Flux changes due to temperature variations for the range of stellar models we consider. The left column shows PHOENIX models relevant to our K0 case, and the right column shows PHOENIX models relevant to our M6 case. The top panels show the spectra in absolute flux units, while the bottom panels show each set normalized to the middle-temperature model in each set. The wavelengths and resolution of the spectra are relevant to NIRSpec/PRISM. Larger flux differences are evident for the set of models relevant to the M6 case, which lead to more successful inferences from the retrievals.*

Detection of an Earth-sized exoplanet orbiting the nearby ultracool dwarf star SPECULOOS-3

Gillon, Michaël; Pedersen, Peter P.; Rackham, Benjamin V.; Dransfield, Georgina ; Ducrot, Elsa; Barkaoui, Khalid; Burdanov, Artem Y.; Schroffenegger, Urs ; Gómez Maqueo Chew, Yilen; Lederer, Susan M. ; Alonso, Roi; Burgasser, Adam J. ; Howell, Steve B. ; Narita, Norio; et al

➔ Nature Astronomy, Volume 8, p. 865-878

Located at the bottom of the main sequence, ultracool dwarf stars are widespread in the solar neighbourhood. Nevertheless, their extremely low luminosity has left their planetary population largely unexplored, and only one of them, TRAPPIST-1, has so far been found to host a transiting planetary system. In this context, we present the SPECULOOS project's detection of an Earth-sized planet in a 17 h orbit around an ultracool dwarf of M6.5 spectral type located 16.8 pc away. The planet's high irradiation (16 times that of Earth) combined with the infrared luminosity and Jupiter-like size of its host star make it one of the most promising rocky exoplanet targets for detailed emission spectroscopy characterization with JWST. Indeed, our sensitivity study shows that just ten secondary eclipse observations with the Mid-InfraRed Instrument/Low-Resolution Spectrometer on board JWST should provide strong constraints on its atmospheric composition and/or surface mineralogy.

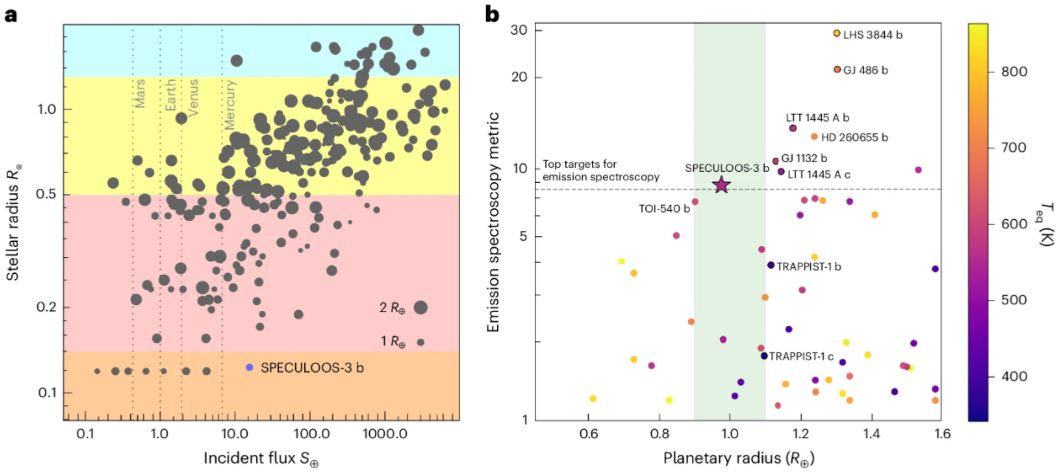

***Figure 4**. **a**, Sizes of host stars in solar radii ($R_{\odot}$) and incident stellar fluxes of known sub-Neptune-sized exoplanets. The sizes of the symbols scale linearly with the radius of the planets. The background is colour-coded according to stellar size (in solar masses), with the UCD regime shown in orange. The red, yellow, and blue shadings show, respectively, the regimes of M-dwarfs, of G-dwarfs and K-dwarfs, and of more massive stars. The positions of the terrestrial Solar System planets are shown for reference. One can see that SPECULOOS-3 b extends the unique planet sample of TRAPPIST-1 to a larger stellar flux. **b**, SPECULOOS-3 b in the context of other known transiting terrestrial exoplanets (with a planetary radius $R_p < 1.6$ Earth radii ($R_{\oplus}$)) that are cool enough (equilibrium temperature $T_{eq} < 880$ K; ref. 34) to have a dayside made of solid rock (in contrast to hotter magma worlds with molten surfaces). The planets are shown as a function of their radius and emission spectroscopy metric (ESM)35. Data points are colour-coded according to their T_{eq}. The shaded green area highlights planetary radii most similar to Earth's (0.9–1.1 $R_{\oplus}$). The dashed horizontal line represents the ESM threshold of 7.5 recommended by ref. 35 to identify the top targets for emission spectroscopy with JWST. SPECULOOS-3 b is one of the smallest planets amenable to emission spectroscopy with MIRI/LRS. Data from ref. 116.*